Nucleation and propagation of brittle fracture as a constrained energy minimization problem

Oscar Lopez-Pamies[a], Farhad Kamarei[a], Gilles A. Francfort[b], Alessandro Giacomini[c]

[a] *Department of Civil and Environmental Engineering, University of Illinois, Urbana–Champaign, IL 61801, USA*
[b] *Flatiron Institute, 162 Fifth Avenue, New York, NY 10010, USA*
[c] *DICATAM, Sezione di Matematica, Università degli Studi di Brescia, Brescia, Italy*

Abstract

This paper presents a macroscopic, or continuum, theory aimed at describing when, where, and why cracks nucleate and propagate in nominally elastic brittle materials under monotonic, quasi-static, but otherwise arbitrary mechanical loads. Motivated by recent insights, the proposed sharp theory posits that: *cracks nucleate and propagate exclusively in regions where the strength surface of the material is exceeded, with their evolution dictated by the minimization of the sum of the potential — the elastic energy minus the work done by the externally applied forces — and surface energies.* While the theory applies to materials with any elasticity (linear or nonlinear) and any material symmetry (isotropic or anisotropic), attention is restricted here to the most basic case of isotropic elastic brittle materials. For demonstration purposes, the theory is confronted with a set of nine tests that span the entire range of well-settled experimental knowledge on fracture nucleation and propagation — the so-called "Nine Circles of Elastic Brittle Fracture" — on both a hard material (a silicate glass) and a soft material (a synthetic rubber).

Key words: Strength, Toughness, Flow and Fracture, Energy Methods

1. Introduction

Over the past decade, we, together with various collaborators, have built a body of research (Kumar et al., 2018a,b; Francfort et al., 2019; Kumar and Lopez-Pamies, 2020; Kumar et al., 2020; Kumar and Lopez-Pamies, 2021; Kumar et al., 2022, 2024; Larsen et al., 2024; Kamarei et al., 2024; Saha et al., 2024; Kamarei et al., 2025, 2026b; Saha et al., 2026b,a; Lopez-Pamies and Kamarei, 2025) suggesting that a comprehensive continuum description of fracture nucleation and propagation in solids is within reach. Building on these efforts, this paper takes a first step toward such an objective by initiating a series aimed at describing when, where, and why cracks nucleate and propagate in nominally elastic brittle materials subjected to mechanical loads. Recall that an elastic brittle material — the most basic idealization of a solid capable of fracture — is one that, in response to mechanical forces, either deforms elastically or creates new surfaces, the latter being the sole mechanism by which it dissipates energy. Specifically, this first paper addresses these questions for the case of monotonic quasi-static loading, deferring non-monotonic and dynamic loading to future work. While the proposed theory is applicable to any elastic constitutive behavior (linear or nonlinear) and material symmetry (isotropic or anisotropic), the present work focuses on the most common setting, that of isotropic elastic brittle materials.

Drawing on over two centuries of experimental observations across a diverse range of materials — including rocks, concrete, ceramics, inorganic and organic glasses, and elastomers — the aforementioned studies have provided the following insights.

Email addresses: pamies@illinois.edu (Oscar Lopez-Pamies), kamarei2@illinois.edu (Farhad Kamarei), gfrancfort@flatironinstitute.org (Gilles A. Francfort), alessandro.giacomini@unibs.it (Alessandro Giacomini)

The first is a precise and complete definition of strength, a macroscopic property that has been historically a subject of mistreatment and misinterpretation; see Subsection 1.1. As in (Kumar and Lopez-Pamies, 2020; Kumar et al., 2020) and as restated in Definition 1.1 below, the strength of an elastic brittle material is defined as the set of all critical stresses[1] $\mathbf{S}$ at which fracture nucleates in a specimen[2] under a state of monotonically increasing, spatially uniform, but otherwise arbitrary stress. This collection of critical stress states defines a surface in stress space, $\mathcal{F}(\mathbf{S}) = 0$, referred to as the *strength surface* of the material.

Then, that elastic brittle fracture necessitates three distinct macroscopic properties: (i) the elasticity of the material; (ii) its strength surface; and (iii) its fracture toughness or critical energy release rate. In particular, for the basic case of isotropic elastic brittle materials, any viable formulation must incorporate the isotropic elastic energy density

$$W(\mathbf{F}) = \varphi(I_1, I_2, J)$$

of the material, its isotropic strength surface

$$\mathcal{F}(\mathbf{S}) = \widehat{\mathcal{F}}(s_1, s_2, s_3) = 0,$$

and its scalar fracture toughness

$$G_c.$$

In these expressions, $\mathbf{F} = \nabla \mathbf{y}$ denotes the gradient of the deformation field $\mathbf{y}$, $I_1 = \operatorname{tr} \mathbf{C}$, $I_2 = \frac{1}{2}(I_1^2 - \operatorname{tr} \mathbf{C}^2)$, and $J = \sqrt{\det \mathbf{C}} = \det \mathbf{F}$ stand for the classical principal invariants associated with the right Cauchy-Green deformation tensor $\mathbf{C} = \mathbf{F}^T\mathbf{F}$, and $s_1 \geq s_2 \geq s_3$ are the principal nominal stresses.

Finally, that fracture itself is governed by a two-fold criterion:

1. Cracks can nucleate or grow only in regions where the strength surface of the material, $\mathcal{F}(\mathbf{S}) = 0$, has been exceeded.

2. Within the regions of strength violation, crack evolution is governed by a minimization of a functional, involving the competition between deformation and surface energies.

Note that the first part implies that the violation of the strength surface is a necessary, albeit *not* sufficient, condition for the nucleation and propagation of fracture. The second part states that sufficiency is provided by an energetic competition within the strength violation regions.

With this in mind, we present in Section 3 the central focus of this paper: a macroscopic, or continuum, theory aimed at describing when, where, and why sharp cracks nucleate and propagate in nominally elastic brittle materials under arbitrary monotonic quasi-static loading conditions.

At present, the theory is limited to time-discrete evolutions, and the corresponding time-continuous formulation remains an open challenge. This is so, in part, because the presence of strength in the theory impacts the amount of energy dissipated and possibly the minimizing principle in the time-continuous framework. The mathematical obstacles are numerous. A first set of mathematical results for well-posedness is presented in Section 4.

As a preliminary, Section 2 analyzes three motivating experiments: a silicate glass specimen in simple tension under both displacement and force control, and the self-weight cantilever bending of a mortar beam. In Section 5, we confront the theory with a set of nine tests spanning the complete spectrum of well-settled experimental knowledge on fracture nucleation and propagation — the so-called "Nine Circles of Elastic Brittle Fracture" introduced in (Kamarei et al., 2026b) — for both a hard material (silicate glass) and a soft material (synthetic rubber). Finally, Section 6 provides a few concluding comments.

[1] Throughout this work, $\mathbf{S}$ denotes the first Piola-Kirchhoff stress tensor.

[2] As for any macroscopic property to make sense, the specimen must be large enough in all of its dimensions to be viewed as a homogeneous piece. What "enough" means for strength will be addressed later in Remark 3.3.

1.1. A brief overview of the history and current understanding of fracture from the continuum point of view

The following overview serves not only to situate the current work within the broader literature of solid mechanics, but also to "*Ἀπόδοτε οὖν τὰ Καίσαρος Καίσαρι* [Render unto Caesar the things which are Caesar's]"[3] and to underscore the tortuous path that research in this area has historically followed. The summary is divided into the three different types of mechanics that govern fracture, each restricted to the monotonic quasi-static loading conditions of interest in this paper: (*i*) the mechanics of deformation; (*ii*) the mechanics of strength; and (*iii*) the mechanics of toughness.

1.1.1. The mechanics of elastic deformation

Fifteen years after Cauchy (1823) had introduced the definition of stress, the equations that describe the deformation of a body made of a linear elastic material were established in their full generality by Green (1838). Prior to Green's work, Navier (1827) and Cauchy (1828), among others, had written the equations, but with a degree of confusion as to material symmetry; see, e.g., the historical account in the classical monograph by Love (1906). Lamé (1852), for his part, did write the equations as they now stand. In an isotropic nonlinear setting, the correct equations were first written by Rivlin (1948a,b) over a century later. Finally, for a body made of a fully anisotropic nonlinear elastic material, the equations were worked out by Truesdell and Noll (1965).

1.1.2. The mechanics of strength

Lamé was first to explicitly mention that the equations of linear elastostatics cease to be valid at sufficiently large loads when the material fractures (Lamé and Clapeyron, 1831). He solved the boundary-value problems of a thick-walled circular cylinder and a thick-walled spherical shell, made of an isotropic linear elastic material, under inner and outer pressures and postulated that the specimens would fracture when the hoop stress at their inner boundary reaches a critical value characteristic of the material, the "tensile strength" of the material. In other words, he posited that when the maximum tensile principal stress at a material point in a structure reaches that value, $s_1 = s_{\mathtt{ts}}$ say, fracture would ensue at that material point. Fracture mechanics from the continuum point of view was born and it was all about nucleation.

About two decades later, Rankine (1858) generalized Lamè's criterion by postulating that fracture would ensue whenever either the maximum tensile or minimum compressive principal stress at a material point in a structure would reach critical values characteristic of the material, the "tensile strength" or "compressive strength", that is, whenever $s_1 = s_{\mathtt{ts}}$ or $s_3 = -s_{\mathtt{cs}}$. He applied this criterion, in particular, to beams subjected to transverse loading. A few years later, Saint-Venant proposed the alternative view that fracture ensues at a material point whenever the maximum tensile principal strain — as opposed to stress — reaches a critical value (Navier, 1864). Mohr (1900) noted that none of the aforementioned criteria could explain experimental observations in general. Instead, he proposed a criterion that depends on the maximum and minimum principal stresses, one of the form $s_1 - s_3 = f(s_1 + s_3)$, where the function $f(\cdot)$ is material specific. Following in his peers' footsteps, Mohr also posited that satisfaction of this criterion at a material point would result in fracture at that point. Mohr's approach was soon shown not to be experimentally viable either (von Kármán, 1911).

The notion of strength at material points continued to dominate the field until the early 1920s, when Griffith (1921, 1924) steered the mechanics community in an entirely new direction, that of fracture propagation and the mechanics of toughness. The shift turned out to be so influential that theoretical studies of fracture nucleation and the mechanics of strength were *de facto* abandoned for nearly a century. A resurgence of the topic took place in the early 2000s, prompted by investigations into fracture nucleation from notches in hard materials (Leguillon, 2002; Cornetti et al., 2006) and cavitation in elastomers (Lefèvre et al., 2015; Breedlove et al., 2024). The latter led to the following definition of strength introduced in (Kumar and Lopez-Pamies, 2020; Kumar et al., 2020) and already mentioned above:

[3] Matthew 22:21.

Definition 1.1. *The strength of an elastic brittle material is the set of all critical stresses* $\mathbf{S}$ *at which the material fractures when it is subjected to a state of monotonically increasing, spatially uniform, but otherwise arbitrary stress. Such a set of critical stresses defines a surface* $\mathcal{F}(\mathbf{S}) = 0$ *in stress space — potentially, any star-shaped surface containing the origin* $\mathbf{S} = \mathbf{0}$ *— which is referred to as the strength surface of the material.*

This definition redresses two early misconceptions. First, that violation of a stress (or strain) condition at a material point implies nucleation of fracture. Experiments show that, for fracture nucleation to occur, the violation of a stress condition has to take place over a sufficiently large subdomain whose size is material dependent. Then, that the stress condition has a universal form. Experimental evidence points to the contrary.

As such, Definition 1.1 says nothing about when fracture nucleates in problems where the stress field is not spatially uniform and thus it says nothing about fracture nucleation at individual material points; as elaborated below, additional criteria are necessary to determine the onset of fracture when the stress state is spatially non-uniform. Definition 1.1 also says nothing about a particular form of the strength surface $\mathcal{F}(\mathbf{S}) = 0$; it simply must be star-shaped and contain $\mathbf{S} = \mathbf{0}$ in its interior.

1.1.3. The mechanics of toughness

The original idea of energy competition. Aware of the inability of the prevailing strength conditions to explain experimental observations, Griffith (1921, 1924) introduced an energy-based approach, positing that fracture is governed by a global energy balance. In his own words (Griffith, 1924, page 55): "*If owing to the action of a stress a crack is formed, or a pre-existing crack is caused to extend, therefore, a quantity of energy proportional to the area of the new surface must be added, and the condition that this shall be possible is that such addition of energy shall take place without any increase in the potential energy of the system* [the sum of the potential energy of the applied forces, the strain energy, and the surface energy of the crack]." Put differently, an elastic brittle body subjected to external loads can either deform elastically or undergo a combined process of elastic deformation and surface creation, both processes being consistent with energy conservation. The process with surface creation involves a redistribution of energy, from deformation energy to surface energy, with the latter being proportional to the area of the newly created surface.

Griffith (1921, 1924) applied his criterion to an elementary problem, which helped clarify three key aspects of his approach. The problem was that of an infinite plate, made of an isotropic linear elastic material, containing a pre-existing straight through-thickness crack, that is subjected to affine biaxial tensile tractions aligned with the crack. The goal was to determine when — that is, at what value of the applied tractions — the crack starts to grow, assuming a straight-ahead trajectory. In his own words (Griffith, 1924, page 57): "*The condition that the crack may extend, that is, that rupture may occur, is then obtained by expressing the condition that the total energy* [the sum of the potential energy of the applied tractions, the strain energy and the surface energy of the crack] *is unchanged by small variations in the length of the crack.*" This reveals three significant aspects of his approach: first, the criterion applies strictly to the infinitesimal growth of pre-existing cracks rather than finite-size growth or fracture nucleation; second, it offers no predictive information regarding the resulting crack path; and third, its application amounts to computing variations of the elastic energy minus the work done by the applied forces with respect to infinitesimal add-cracks along a pre-supposed crack path, a quantity that is now classically denoted as G and referred to as the energy release rate.

The physical meaning of G_c*.* Griffith (1921, 1924) postulated that the constant of proportionality multiplying the area of the newly created surface in the global energy balance was twice the surface tension of the material (at interfaces with air). Recognizing that this choice often underestimated experimental measurements, Orowan (1948), Irwin (1948), and Rivlin and Thomas (1953) independently proposed a broader definition. They argued that the proportionality constant should represent the total energy, per unit undeformed area, expended during the fracture process. This material property — measurable through macroscopic testing — is currently denoted as G_c and referred to as the critical energy release rate or fracture toughness.

Equivalency of G and stress intensity factors. In 1957, seeking to better understand the local implications of the global energy balance proposed by Griffith, within the setting of 2D isotropic linear elastostatics, Irwin (1957) established that the energy release rate G — again, associated with a pre-supposed crack path — can be expressed in terms of the so-called stress intensity factors, the coefficients in the leading singular terms of the stress field at a crack front. The equivalency between the energy release rate (global perspective) and the crack front singularities (local perspective) was shown to hold true more generally in 3D and isotropic finite elastostatics in subsequent works (e.g., Rice, 1966; Knowles and Sternberg, 1972, 1973; Budiansky and Rice, 1973). This insight provided by Irwin (1957) sparked a vast body of research dedicated to characterizing stress intensity factors across diverse geometries, materials, and loading conditions. Although predominantly focused on isotropic linear elastostatics, this pursuit remains active today and has resulted in reference handbooks; see, e.g., (Tada et al., 1973).

Equivalency of G and the J-integral. In a related contribution published in 1968, within the setting of 2D isotropic small-strain but possibly nonlinear elastostatics, Rice (1968) established that the energy release rate G can additionally be expressed in terms of a path-independent integral, the J-integral, arising out of material invariances. Later works showed that such path-independent integrals can be worked out more generally in 3D and isotropic finite elastostatics (e.g., Knowles and Sternberg, 1972; Budiansky and Rice, 1973). Because it makes the determination of G more palatable, the computation of the J-integral has become a standard feature in many commercial FE packages.

Crack path based on the stress field around the crack front. By the early 1960s, numerous comparisons with experiments on different materials had demonstrated an apparent validity of Griffith's idea of energy competition to describe and predict when a large[4] pre-existing crack starts to grow along a crack path that is known *a priori*. The focus then turned to the prediction of the crack path. Starting with the work of Erdogan and Sih (1963), who, motivated by their own experiments on PMMA, proposed the so-called Maximum Tangential Stress criterion, a slew of criteria based on the local stress fields around crack fronts were, and continue to be put forth; see, e.g., (Sih, 1974; Goldstein and Salganik, 1974; Nuismer, 1975; Palaniswamy and Knauss, 1978; Wu, 1978; Theocaris and Andrianopoulos, 1982; Tian et al., 1982) and the reviews (Qian and Fatemi, 1996; Hua et al., 2023). Most of them only apply to isotropic linear elastic brittle materials in 2D settings. Comparisons with the many experiments that have been carried out to probe nontrivial crack paths in a variety of materials seem to indicate that none of these have a universal character (Panasyuk et al., 1965; Palaniswamy and Knauss, 1978; Williams and Ewing, 1972; Ueda et al., 1983; Royer, 1986; Richard, 1985; Mahajan and Ravi-Chandar, 1989; Davenport and Smith, 1993; Richard et al., 2014). Also none are amenable to generalizations to nonlinear elastic and anisotropic materials in a 3D setting.

The variational approach to fracture. At the end of the 1990s, Francfort and Marigo (1998) introduced a new idea to describe crack path within the setting of linear elastic brittle materials subject to mixed Dirichlet and zero Neumann boundary conditions and in the absence of body forces. In a nutshell, the fracture state in a body is viewed as a global minimization problem for the sum of the elastic and surface energies with arbitrary add-cracks as test fields. This variational approach is in line with Griffith's original idea of energy competition and is amenable to generalizations to nonlinear elastic and anisotropic materials in a 3D setting (Bourdin et al., 2008). In addition to describing the crack path, the formulation transcends the limitations of Griffith's approach in two additional ways. First, the growth of pre-existing cracks need not be infinitesimal, instead, finite-size crack growth is possible. Second, crack nucleation is also possible as a direct result of the global energy minimization.

It became clear over time that the global energy minimization approach can yield results that are inconsistent with experimental evidence. It also became clear that replacing global energy minimization with some type of local minimization (e.g., Chambolle et al., 2008, 2009, 2010; Larsen, 2024) was not a cure.

[4] "Large" refers to large relative to the characteristic size of the underlying heterogeneities in the material at hand. By the same token, "small" refers to sizes that are of the same order or just moderately larger than the sizes of the heterogeneities.

A further limitation of the variational approach is its apparent inability to handle non-zero Neumann boundary conditions and/or body forces. An attempt at removing this limitation was recently proposed by Larsen (2021) but it yields a formulation that is inconsistent with experimental observations. Moreover, it does not reduce to the usual formulation in the case of zero Neumann boundary conditions.

The current view: Energy minimization constrained by strength. In 2025, guided by the two-fold criterion stated above, two of us (Lopez-Pamies and Kamarei, 2025) introduced the following tenet: the growth of a large crack takes place within and only within regions where the strength surface of the material has been exceeded, this in a manner such that the sum of the potential and surface energies is minimized.

The tenet for the growth of large cracks introduced there serves as a precursor to the theory of fracture nucleation and propagation proposed in this work.

2. Illustrating the concept

2.1. The simple tension test of a silicate glass specimen: Fracture under displacement control

One of the simplest possible illustrations of the proposed framework is that of a specimen that is subjected to simple tension until a crack nucleates and subsequently propagates severing the specimen into two pieces.

For this type of test, experiments show a monotonic force-displacement (P vs. u) response up to a critical state (u_c, P_c) at which point a crack orthogonal to the loading direction appears and severs the specimen[5] and this irrespective of whether the specimen is pulled via an applied displacement u or an applied force P; see Fig. 1. The post-critical behavior depends on how the specimen is pulled. Under displacement control, the force jumps from $P = P_c$ to $P = 0$ at u_c. Under force control, it is the displacement that jumps beyond $u = u_c$, leading to a loss of elastostatic equilibrium as the specimen fails. We examine displacement control in this subsection and force control in the next.

For definiteness, we consider the test schematically depicted in Fig. 1. It consists of a thin rectangular specimen, of length $L = 1.5$ mm, width $H = 0.75$ mm, and thickness $B = 0.15$ mm, that is firmly gripped at the opposite ends of its length and pulled in tension. These small sizes are purposely selected to better illustrate key aspects of the problem. Denoting the laboratory Cartesian frame of reference by $\{\mathbf{e}_1, \mathbf{e}_2, \mathbf{e}_3\}$, the specimen occupies the open bounded domain $\Omega_0 = \{\mathbf{X} : 0 < X_1 < L, |X_2| < H/2, |X_3| < B/2\}$. The specimen is assumed to be made of a typical silicate (soda-lime) glass with the classical elastic energy density

$$W(\mathbf{F}) = \mu \operatorname{tr} \mathbf{E}^2 + \frac{\Lambda}{2}(\operatorname{tr} \mathbf{E})^2 \tag{1}$$

of an isotropic linear elastic material, Drucker-Prager strength surface

$$\mathcal{F}(\mathbf{S}) = \sqrt{\mathcal{J}_2} + \frac{s_{\mathtt{cs}} - s_{\mathtt{ts}}}{\sqrt{3}\,(s_{\mathtt{cs}} + s_{\mathtt{ts}})}\,\mathcal{I}_1 - \frac{2 s_{\mathtt{cs}} s_{\mathtt{ts}}}{\sqrt{3}\,(s_{\mathtt{cs}} + s_{\mathtt{ts}})} = 0, \tag{2}$$

and scalar fracture toughness G_c. The values of the material constants are in Table 1. In expressions (1) and (2), $\mathbf{E}(\mathbf{u}) = 1/2(\mathbf{F} + \mathbf{F}^T - 2\mathbf{I}) = 1/2(\nabla \mathbf{u} + \nabla \mathbf{u}^T)$ denotes the symmetrized gradient of the displacement field $\mathbf{u} = \mathbf{y} - \mathbf{X}$, or infinitesimal strain tensor, μ and Λ are the Lamé constants, $\mathcal{I}_1 = s_1 + s_2 + s_3$, $\mathcal{J}_2 = 1/3(s_1^2 + s_2^2 + s_3^2 - s_1 s_2 - s_1 s_3 - s_2 s_3)$, while $s_{\mathtt{ts}}$ and $s_{\mathtt{cs}}$ stand for the uniaxial tensile and compressive strengths, that is, they denote the critical nominal stress values at which fracture nucleates under uniform states of monotonically increased uniaxial tension $\mathbf{S} = \operatorname{diag}(s > 0, 0, 0)$ and compression $\mathbf{S} = \operatorname{diag}(-s < 0, 0, 0)$, respectively.

Now, the two-fold criterion for fracture recalled in the Introduction suggests several plausible formulations of sharp fracture. The simplest among these is the following: a sharp crack nucleates within and only within

[5] Note that no direct experimental evidence has yet shown whether crack nucleation occurs simultaneously across the entire specimen or — as is more likely — begins in a subdomain and then propagates rapidly. This is due to the exact locus of crack nucleation being sensitive to spatial variations in strength (resulting from the inherent randomness of material defects), compounded by a fracture process that occurs too rapidly for conventional high-speed imaging to resolve.

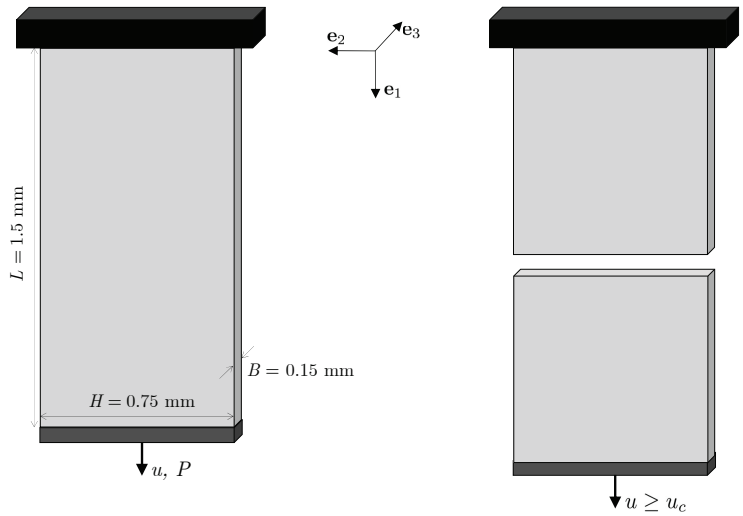


Figure 1: Schematic of the simple tension test on a silicate glass specimen examined in this and the next subsections: (left) initial undeformed configuration and applied loading; (right) fractured state following the nucleation and propagation of a crack orthogonal to the loading axis.

Table 1: Material constants for the silicate glass used throughout this work.

Elasticity constants	μ (GPa)	Λ (GPa)	E (GPa)	ν
	28.7	22.5	70	0.22
Strength constants	$s_{\mathtt{ts}}$ (MPa)	$s_{\mathtt{cs}}$ (MPa)		
	40	1000		
Fracture toughness	G_c (N/m)			
	10			

the region where the strength surface $\mathcal{F}(\mathbf{S}) = 0$ of the material is exceeded in a way that the sum of the potential and surface energies

$$\mathcal{E} = \int_{\Omega_0 \setminus \Gamma} W(\mathbf{F})\, \mathrm{d}\mathbf{X} - \int_{\Omega_0 \setminus \Gamma} \mathbf{b} \cdot \mathbf{y}\, \mathrm{d}\mathbf{X} - \int_{\partial\Omega_0^{\mathcal{N}}} \overline{\mathbf{s}} \cdot \mathbf{y}\, \mathrm{d}\mathcal{H}^2 + G_c \mathcal{H}^2(\Gamma) \tag{3}$$

is minimized among all possible test cracks Γ, this while elastostatic equilibrium is satisfied. Here, neglecting the minor effects of the body force due to gravity and the atmospheric pressure, $\mathbf{b} = \mathbf{0}$ and $\overline{\mathbf{s}} = \mathbf{0}$, while $\mathcal{H}^2(\Gamma)$ denotes the 2-dimensional Hausdorff measure (the surface measure) of the unknown crack.

We begin by numerically determining (via finite elements[6] and assuming plane-stress conditions) the critical global strain at which the strength condition $\mathcal{F}(\mathbf{S}) \geq 0$ is first satisfied. For definiteness, we assume the presence of a weaker central circular region with a 0.65 mm diameter where the uniaxial tensile strength is 10% lower ($s_{\mathtt{ts}} = 40$ MPa) than the surrounding material ($s_{\mathtt{ts}} = 44$ MPa). The calculations show that the condition $\mathcal{F}(\mathbf{S}) \geq 0$ is first reached at the specimen's corners — due to stress concentrations near the grips — and then within the central circular region of reduced strength, the latter first occurring at $u/L = 5.7 \times 10^{-4}$, as shown in Fig. 2(a). It is in this central region — and not at the corners — that a configuration with

[6]In this paper, all finite-element simulations for glass and mortar were carried out with quadratic simplicial elements. For rubber, they were carried out with conforming quadratic Crouzeix-Raviart elements (Crouzeix and Raviart, 1973); see also the Appendix in (Lefèvre and Lopez-Pamies, 2017).

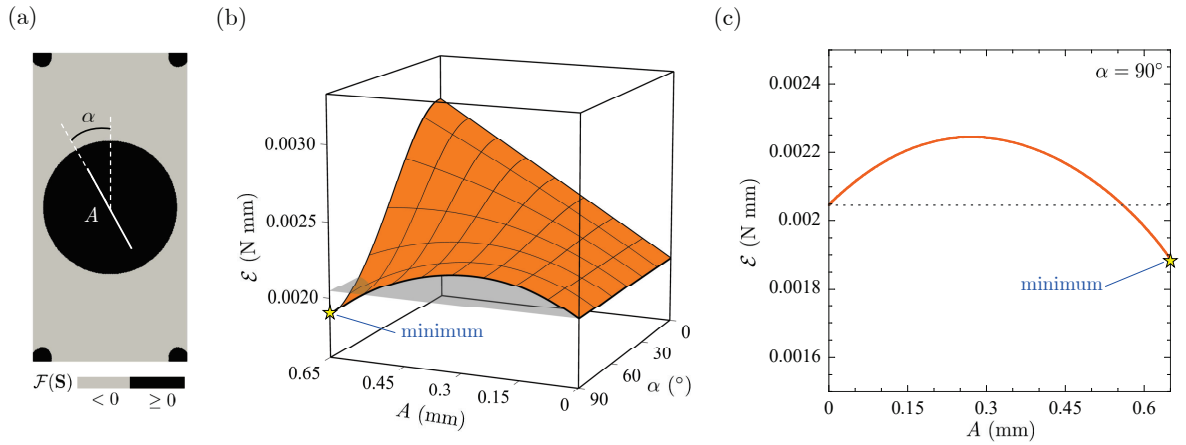


Figure 2: Elastic simulations of the tension test, at the applied global strain $u/L = 5.7 \times 10^{-4}$, on silicate glass containing test cracks of lengths $A \in [0, 0.65\,\text{mm}]$, thickness $B = 0.15$ mm, oriented at angles $\alpha \in [0°, 90°]$ with respect to the direction of the applied tension. (a) Contour plot of the regions of the specimen where the stress field exceeds ($\mathcal{F}(\mathbf{S}) \geq 0$) the strength surface of the material, depicting the test cracks considered within. (b) The energy $\mathcal{E}$ of the specimen plotted as a function of the test crack length A and angle α. (c) The cross section of $\mathcal{E}$ for fixed crack angle $\alpha = 90°$ as a function of A.

a crack can outcompete the initial uncracked configuration. At $u/L = 5.7 \times 10^{-4}$, we then numerically determine the energy (3) for specimens containing straight through-thickness test cracks, $\Gamma = \Gamma(A, \alpha)$, of crack length A, so that $\mathcal{H}^2(\Gamma) = AB$, and crack orientation α relative to the applied tension; see Fig. 2(a). This crack topology is chosen for its consistency with experimental observations. Figure 2(b) presents the numerical results obtained for the energy $\mathcal{E}$ as a function of A and α, while Fig. 2(c) presents a cross section of $\mathcal{E}$ as a function of A at the fixed crack angle $\alpha = 90°$.

The results in Fig. 2 offer the following insights. First, the crack of length $A = 0.65$ mm — the largest possible length that can be fitted within the strength violation region — oriented at $\alpha = 90°$ minimizes the energy $\mathcal{E}$. This implies that such a crack nucleates at $u/L = 5.7 \times 10^{-4}$. Crucially, observe that the proposed constrained energy minimization delivers both the when ($u/L = 5.7 \times 10^{-4}$) and the where ($A = 0.65$ mm and $\alpha = 90°$) of crack nucleation.

Second, if the strength violation occurs over a region with diameter smaller than $\ell_{\texttt{ts}} = 0.54$ mm, the energy is minimized at $A = 0$, meaning no crack nucleates. This threshold defines a length scale below which strength (in this case, the uniaxial tensile strength $s_{\texttt{ts}}$) can no longer be treated as a macroscopic material property. This scale is comparable to, though distinct from, the classical material length scale $EG_c/s_{\texttt{ts}}^2 = 0.44$ mm. As elaborated in the next section, such length scales arise from the dimensional interplay between elasticity ($force/length^2$), strength ($force/length^2$), and toughness ($force/length$) entering as material inputs in the constrained energy minimization.

Third, if the strength violation occurs over a region larger than 0.65 mm in diameter, the energy would be minimized again by the largest possible crack that fits within that region at 90°. In particular, if the region is the entire specimen, the energy would be minimized by a severing crack at 90°.

Fourth, the minimizing energy ($\mathcal{E} = 0.00189$ N mm) for the configuration with the nucleated crack is smaller than the elastic energy ($\mathcal{E} = 0.00205$ N mm) for the configuration without the crack prior to nucleation; the latter is indicated by a grey plane in Fig. 2(b) and a dashed line in Fig. 2(c). An abrupt drop in the (quasi)-static energy functional occurs. It is not clear to us at present if the violation of the strength is accompanied by an additional dissipation which manifests itself whenever there is a jump in crack size (at the time of nucleation of a finite-size crack for example). In any case, in the setting of uniaxial traction, the nucleation of a severing crack will trigger dynamic effects that consume energy. If the material dissipates energy by deformation when loaded dynamically (e.g., via viscous processes) and/or the specimen is immersed in a dissipative surrounding medium like air, kinetic energy will eventually be

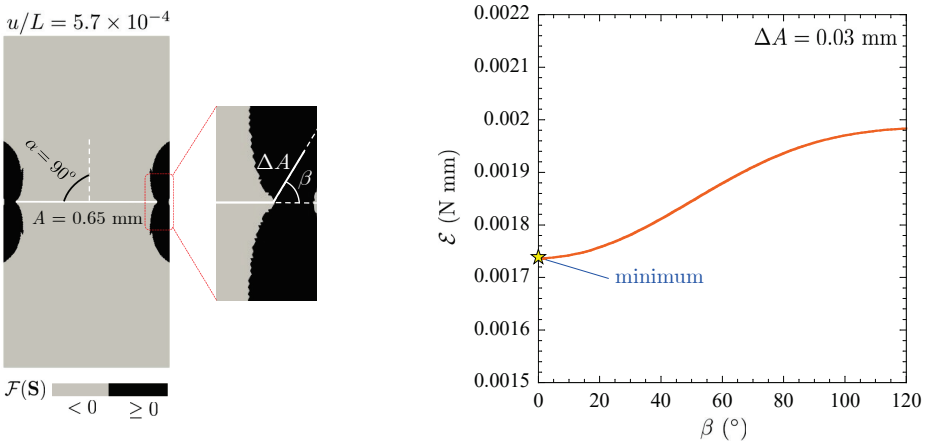


Figure 3: Elastic simulations of the tension test, at the applied global strain $u/L = 5.7 \times 10^{-4}$, on silicate glass containing the initial minimizing crack, ($A = 0.65\,\text{mm}$, $\alpha = 90°$), with test add-cracks of length ΔA oriented at angles β with respect to the initial crack orientation. The contour plot illustrates the regions of the specimen where the stress field exceeds ($\mathcal{F}(\mathbf{S}) \geq 0$) the strength surface of the material, depicting the test add-cracks considered within. The line plot shows the variation of the energy $\mathcal{E}$ with respect to the add-crack angle β for the fixed add-crack length $\Delta A = 0.03$ mm.

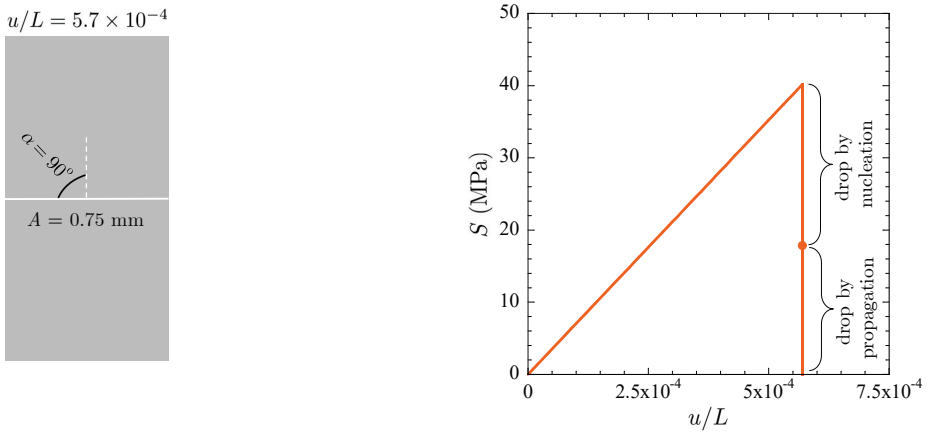


Figure 4: Theoretical prediction of the tension test on silicate glass under displacement control. The results show the global stress $S = P/(BH)$ as a function of the applied global strain u/L, as well as a depiction of the fractured state of the specimen following the nucleation and propagation of a crack orthogonal to the direction of applied tension.

dissipated. Without such dissipation mechanisms, the specimen will not regain static equilibrium, rendering the quasi-static assumption invalid.

Assuming that the quasi-static assumption remains valid after fracture nucleation, we now examine the minimizing solution with crack length $A = 0.65$ mm and crack angle $\alpha = 90°$. Following the previously established procedure, we numerically identify the regions where the strength criterion is exceeded ($\mathcal{F}(\mathbf{S}) \geq 0$) at the applied global strain of $u/L = 5.7 \times 10^{-4}$. As illustrated by the contour plot in Fig. 3, the strength violation is now localized near the crack fronts. Within these updated violation regions, we consider straight through-thickness test add-cracks, $\Gamma = \Gamma(A + 2\Delta A, \alpha, \beta)$, of add-crack length ΔA, so that $\mathcal{H}^2(\Gamma) = (A+2\Delta A)B$, and add-crack orientation β relative to the initial crack orientation; see the schematic depictions in Fig. 3. Numerical results analogous to those presented in Fig. 2(b) show that the energy is minimized at $\Delta A = 0.03$ mm and $\beta = 0°$. Fig. 3 includes a cross section of $\mathcal{E}$ as a function of β for the fixed add-crack length $\Delta A = 0.03$ mm. That is, the constrained minimization dictates that the nucleated crack at

$u/L = 5.7 \times 10^{-4}$ does not stay put, instead it propagates by a finite-size growth in the direction orthogonal to the applied tension.

Repeating the procedure once again leads to a crack, orthogonal to the direction of applied tension, that completely severs the specimen at $u/L = 5.7 \times 10^{-4}$. This is shown by Fig. 4, which also shows the associated global S vs. u/L response of the specimen. This result is consistent with experimental observations. Interestingly, it reveals that the manner in which a specimen under simple tension severs is by the nucleation of a finite-size crack in the region where the strength is weakest, followed by brutal crack propagation.

In the scenario where the region of weakest strength spans the entire width of the specimen, the specimen would fracture via the nucleation of a severing crack.

2.2. The simple tension test of a silicate glass specimen: Fracture under force control

We now consider the test under force control, when the force P is applied instead of the displacement u. In this case, the traction at the bottom grip $\{\mathbf{X} : X_1 = L, |X_2| < H/2, |X_3| < B/2\}$ in the energy functional (3) is no longer zero but such that

$$-\int_{\partial\Omega_0^{\mathcal{N}}} \bar{\mathbf{s}} \cdot \mathbf{y} \, \mathrm{d}\mathcal{H}^2 = -P(u + L). \tag{4}$$

Figure 5 shows results analogous to those presented in Fig. 2 for applied displacement. The main difference is that the value of the energy functional (3) is negative due to the work done (4) by the applied boundary force. Otherwise, the energy functional is essentially the same in terms of the crack length A and the crack angle α. In particular, the crack of largest possible length $A = 0.65$ mm oriented at $\alpha = 90^\circ$ is again the minimizing configuration.

Now, as previously noted, the response of the specimen is independent of the type of loading — be it displacement or force — up until crack nucleation. Post-nucleation, however, the response is fundamentally dictated by the specific boundary condition applied. Figure 6 compares the initial post-nucleation response of the tension test on silicate glass carried out under displacement and force control. Observe that the global stress jumps from $S = 40$ MPa to $S_{\text{J}} = 17.85$ MPa when the crack with length $A = 0.65$ mm and angle $\alpha = 90^\circ$ nucleates at $u/L = 5.7 \times 10^{-4}$ under displacement control. On the other hand, the global displacement jumps from $u/L = 5.7 \times 10^{-4}$ to $u_{\text{J}}/L = 1.27 \times 10^{-3}$ when the crack nucleates at $S = 40$ MPa

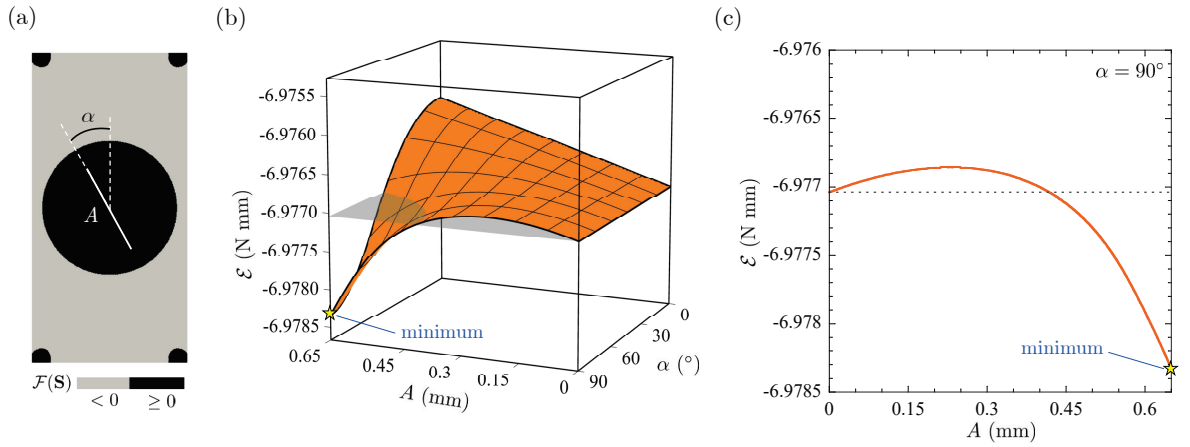


Figure 5: Elastic simulations of the tension test, at the applied global stress $S = 40$ MPa, on silicate glass containing test cracks of lengths $A \in [0, 0.65\,\text{mm}]$, thickness $B = 0.15$ mm, oriented at angles $\alpha \in [0^\circ, 90^\circ]$ with respect to the direction of the applied tension. (a) Contour plot of the regions of the specimen where the stress field exceeds ($\mathcal{F}(\mathbf{S}) \geq 0$) the strength surface of the material, depicting the test cracks considered within. (b) The energy $\mathcal{E}$ of the specimen plotted as a function of the test crack length A and angle α. (c) The cross section of $\mathcal{E}$ for fixed crack angle $\alpha = 90^\circ$ as a function of A.

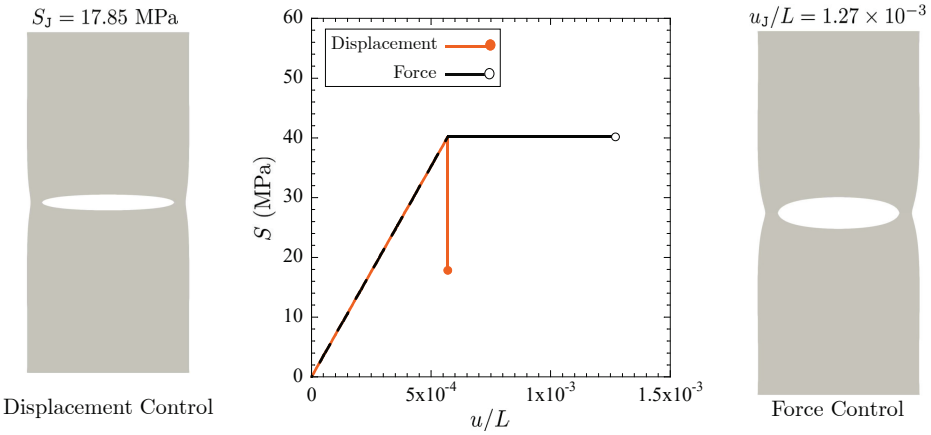


Figure 6: Comparison of the post-nucleation response in the tension test on silicate glass carried out under displacement and force control. The line plot shows that the global S vs. u/L results are identical up until crack nucleation ($A = 0.65\,\text{mm}$, $\alpha = 90°$). Once the crack has nucleated, the global stress jumps from $S = 40$ MPa to $S_J = 17.85$ MPa at $u/L = 5.7 \times 10^{-4}$ under displacement control, while under force control it is the global strain that jumps from $u/L = 5.7 \times 10^{-4}$ to $u_J/L = 1.27 \times 10^{-3}$ at $S = 40$ MPa. The left and right images show the deformed configurations (magnified 100× for better visualization) of the specimens with the crack.

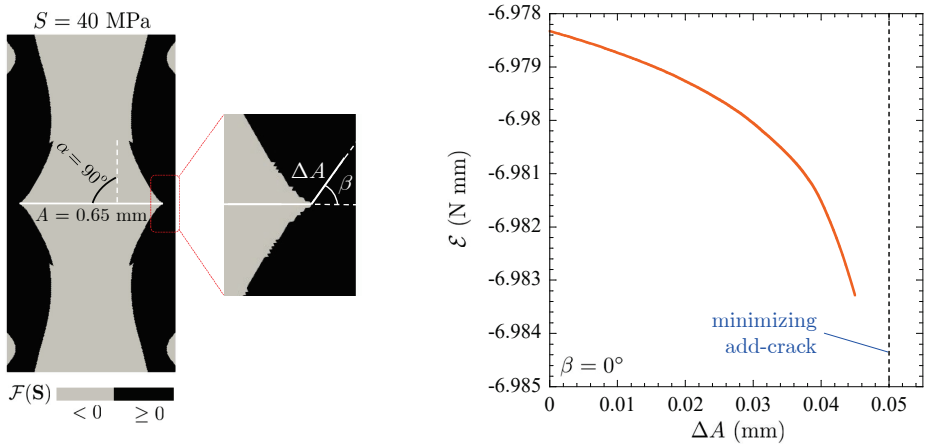


Figure 7: Elastic simulations of the tension test, at the applied global stress $S = 40$ MPa, on silicate glass containing the initial minimizing crack, ($A = 0.65\,\text{mm}, \alpha = 90°$), with test add-cracks of length ΔA oriented at angles β with respect to the initial crack orientation. The contour plot illustrates over the undeformed configuration the regions of the specimen where the stress field exceeds ($\mathcal{F}(\mathbf{S}) \geq 0$) the strength surface of the material, depicting the test add-cracks considered within. The line plot shows the variation of the energy $\mathcal{E}$ with respect to the add-crack length ΔA for $\beta = 0°$.

under force control. Figure 6 includes images — magnified 100× for better visualization — of the deformed configurations of both specimens, helping to visualize the disparity in the resulting jumps.

Figure 7 shows results analogous to those presented in Fig. 3 for applied displacement. It is immediately apparent that the updated region of strength violation for the configuration with the minimizing crack ($A = 0.65\,\text{mm}$, $\alpha = 90°$) is significantly larger than that found for the case of applied displacement. Notably, the region extends from the crack fronts all the way to the lateral boundary of the specimen. Within these updated violation regions, we consider straight through-thickness test add-cracks, $\Gamma = \Gamma(A + 2\Delta A, \alpha, \beta)$, of add-crack length ΔA, so that $\mathcal{H}^2(\Gamma) = (A + 2\Delta A)B$, and add-crack orientation β relative to the initial crack orientation; see the schematic depictions in Fig. 7. The numerical results for the energy $\mathcal{E}$ for $\beta = 0°$ are plotted in Fig. 7 as a function of ΔA from $\Delta A = 0$ to $\Delta A = 0.045$ mm. While results for $\Delta A > 0.045$ mm

are difficult to compute reliably, they are such that $\mathcal{E}$ continues to decrease monotonically as ΔA increases, becoming unbounded as $\Delta A \nearrow 0.05$ mm — that is, as the add-crack approaches the severing of the specimen. Consequently, the constrained minimization dictates that the nucleated crack at $S = 40$ MPa does *not* stay put, instead it propagates by a finite-size growth in the direction orthogonal to the applied tension, severing the specimen. This result is, again, consistent with experimental observations.

As a final remark, following the complete severance of the specimen, the lower subdomain subjected to the applied force undergoes full elastic unloading and rigid-body translation, while the gripped upper subdomain unloads elastically. As elaborated below, in general, severed subdomains may or may not retain stored elastic energy, and could undergo further rigid-body translation and rotation. Regardless, each severed subdomain will subsequently deform and fracture independently. Consequently, they must be treated as separate, independent problems during any subsequent loading, should such loading be possible.

2.3. The cantilever bending test of a mortar beam: Fracture under body forces (self-weight)

Having considered examples where fracture is driven by an applied displacement and an applied traction, we now turn to an example where fracture is driven by a body force.

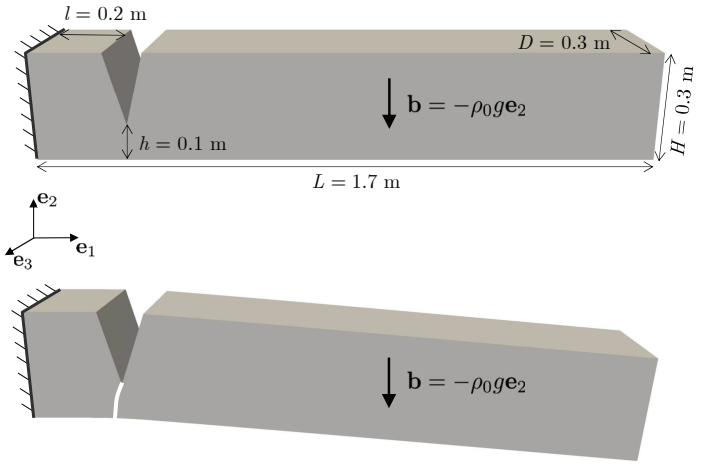


Figure 8: Schematic of the cantilever bending test of a mortar beam examined in this subsection: (top) initial undeformed configuration and applied gravitational body force; (bottom) fractured state following the nucleation of a crack from the notch front and subsequent propagation.

Specifically, we consider the experiment recently introduced in (Kamarei et al., 2026a), schematically depicted in Fig. 8. The setup consists of a beam with length $L = 1.7$ m, height $H = 0.3$ m, and depth $D = 0.3$ m, containing a 30° V-notch located at $l = 0.2$ m from the left boundary and $h = 0.1$ m from the bottom edge. The beam is fully clamped at its left boundary to form a cantilever and is subjected to the body force of gravity, which in our frame of reference reads $\mathbf{b} = -\rho_0 g \mathbf{e}_2$, where ρ_0 is the material mass density and g is the gravitational acceleration. The setup is purposely designed so that a crack nucleates from the notch front and rapidly propagates toward the bottom edge, severing the beam; see Fig. 8.

Here, the beam is assumed to be made of the 3D-printable mortar investigated in (Saha et al., 2026a). It is characterized by the mass density ρ_0, elastic energy density (1), strength surface (2), and fracture toughness G_c, with the values of the various material constants listed in Table 2. In this case, note that the contribution of the body force in the energy functional (3) specializes to

$$-\int_{\Omega_0} \mathbf{b} \cdot \mathbf{y} \, \mathrm{d}\mathbf{X} = \rho_0 g \int_{\Omega_0} y_2 \, \mathrm{d}\mathbf{X}.$$

In the results that follow, for computational expediency, we apply the load by monotonically increasing the gravitational acceleration from $g = 0$ m/s^2 and assume plane-strain conditions. In the actual experiment,

Table 2: Material constants for the mortar used in this subsection.

Mass density	ρ_0 (kg/m^3)			
	2210			
Elasticity constants	μ (GPa)	Λ (GPa)	E (GPa)	ν
	10.7	5.5	25	0.17
Strength constants	$s_{\mathtt{ts}}$ (MPa)	$s_{\mathtt{cs}}$ (MPa)		
	5	48		
Fracture toughness	G_c (N/m)			
	20			

given that the gravitational acceleration is fixed at $g = 9.81$ m/s^2, the right free end of the beam is initially supported from the bottom. This support is gradually lowered and removed, allowing the beam to approach a state where it is subjected to its own self-weight. A 3D simulation of this exact loading process is reported in (Kamarei et al., 2026a), yielding results that are not fundamentally different from the 2D results for the simpler loading process presented here.

As in the previous two examples, we incrementally increase the load, in this case the gravitational acceleration g, to numerically identify the regions where the strength surface is violated, $\mathcal{F}(\mathbf{S}) \geq 0$. Such regions are, as expected, localized around the front of the notch as well as near the clamped edges of the beam. At each increment, we determine the energy (3) for configurations containing straight through-thickness test cracks, $\Gamma = \Gamma(A, \alpha)$, of crack length A, and hence surface area $\mathcal{H}^2(\Gamma) = AD$, emanating from the notch front and oriented at an angle α relative to the direction of gravity; see Fig. 9. Again, this crack topology is chosen for its consistency with experimental observations. Figure 9(b) presents the numerical results obtained for the energy $\mathcal{E}$ as a function of A and α, while Fig. 9(c) presents a cross section of $\mathcal{E}$ as a function of A at the fixed crack angle $\alpha = -5°$. These results pertain to $g = 7.42\,\text{m/s}^2$, which is the critical value at which a configuration containing a crack first minimizes (3). The minimizing crack is one of length

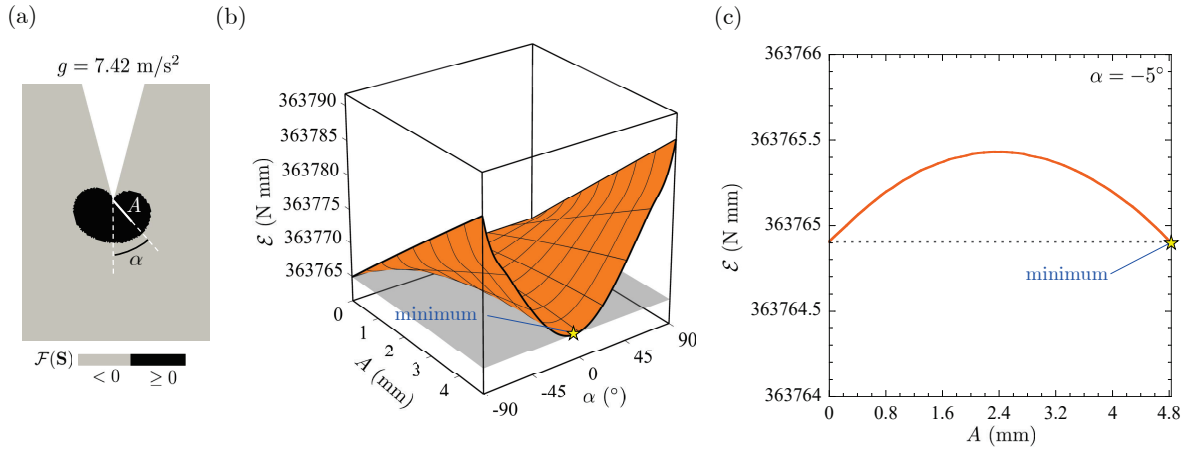


Figure 9: Elastic simulations of the cantilever bending test, at the applied gravitational acceleration $g = 7.42$ m/s^2, on mortar containing test cracks of length A, thickness $D = 0.3$ m, oriented at angles α with respect to the direction of the applied gravitational body force. (a) Contour plot of a magnified region of the specimen where the stress field exceeds ($\mathcal{F}(\mathbf{S}) \geq 0$) the strength surface of the material, depicting the test cracks considered within. (b) The energy $\mathcal{E}$ of the beam plotted as a function of the test crack length A and angle α. (c) The cross section of $\mathcal{E}$ for fixed crack angle $\alpha = -5°$ as a function of A.

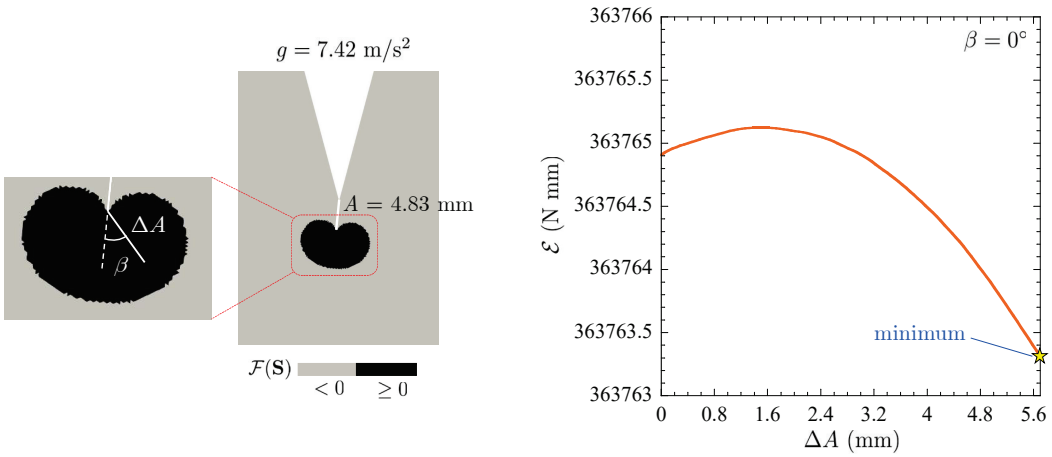


Figure 10: Elastic simulations of the cantilever bending test, at the applied gravitational acceleration $g = 7.42$ m/s^2, on mortar containing the initial minimizing crack, $(A = 4.83\,\text{mm}, \alpha = -5°)$, with test add-cracks of lengths ΔA oriented at angles β with respect to the initial crack orientation. The contour plot illustrates over the undeformed configuration a magnified region of the specimen where the stress field exceeds $(\mathcal{F}(\mathbf{S}) \geq 0)$ the strength surface of the material, depicting the test add-cracks considered within. The line plot shows the variation of the energy $\mathcal{E}$ with respect to the add-crack length ΔA for $\beta = 0°$.

$A = 4.83$ mm oriented at $\alpha = -5°$. Again, this implies that such a crack nucleates at $g = 7.42\,\text{m/s}^2$.

We next analyze the minimizing solution with crack length $A = 4.83$ mm oriented at $\alpha = -5°$. At the critical gravitational acceleration $g = 7.42\,\text{m/s}^2$, we numerically evaluate the regions where the stress field violates the strength surface, $\mathcal{F}(\mathbf{S}) \geq 0$. As shown in Fig. 10, this strength violation localizes around the crack front. Within this updated domain of strength violation, we evaluate straight through-thickness test add-cracks, $\Gamma = \Gamma(A + \Delta A, \alpha, \beta)$, of add-crack length ΔA oriented at an angle β relative to the original crack orientation, resulting in a total crack surface area of $\mathcal{H}^2(\Gamma) = (A + \Delta A)D$. Our energy calculations indicate that $\mathcal{E}$ is minimized for $\Delta A = 5.7\,\text{mm}$ and $\beta = 0°$; see Fig. 10. This result indicates that upon nucleation at $g = 7.42\,\text{m/s}^2$, the crack does not stay put, but instead experiences finite-size growth along its initial trajectory. Subsequent calculations demonstrate that the crack continues its downward propagation until fully severing the beam, in agreement with experimental observations (Kamarei et al., 2026a).

3. The theory: A constrained energy minimization problem

As anticipated in the preceding section, we propose the following principle:

Cracks nucleate and propagate exclusively in regions where the strength surface of the material is exceeded, with their evolution dictated by the minimization of the sum of the potential and surface energies.

At present, we cannot offer a time-continuous formulation, most notably because the propriety of introducing a strength-related dissipation that would be activated at discontinuity times of the crack evolution is yet undecided. Thus the formulation will only be made explicit at a finite set of times $t_k \in \{0 = t_0 < t_1, \ldots < t_m < t_{m+1}, \ldots < t_M = T\}$.

In the case of an isotropic elastic brittle material occupying an open bounded domain $\Omega_0 \subset \mathbb{R}^3$ in its undeformed and stress-free configuration, the theory, in its time-discretized version, can be cast as follows. We denote by $\mathbf{b}(\mathbf{X}, t)$ the time-dependent body force, $\bar{\mathbf{s}}(\mathbf{X}, t)$ the time-dependent nominal traction on the Neumann part $\partial\Omega_0^{\mathcal{N}}$ of the boundary $\partial\Omega_0$, both of which we assume to be dead loads for simplicity sake, and $\bar{\mathbf{y}}(\mathbf{X}, t)$ the time-dependent deformation prescribed on the Dirichlet part $\partial\Omega_0^{\mathcal{D}}$ of the boundary $\partial\Omega_0$. We write

$$\mathcal{P}(\mathbf{y}, \Gamma) := \int_{\Omega_0 \setminus \Gamma} W(\nabla \mathbf{y})\, \mathrm{d}\mathbf{X} - \int_{\Omega_0 \setminus \Gamma} \mathbf{b}_k \cdot \mathbf{y}\, \mathrm{d}\mathbf{X} - \int_{\partial\Omega_0^{\mathcal{N}}} \bar{\mathbf{s}}_k \cdot \mathbf{y}\, \mathrm{d}\mathcal{H}^2 \tag{5}$$

for the potential energy, at times t_k. Then, the pair deformation field-crack set $(\mathbf{y}_k = \mathbf{y}_k(\mathbf{X}), \Gamma_k)$ minimizes

$$\mathcal{E}(\mathbf{y}, \Gamma) := \mathcal{P}(\mathbf{y}, \Gamma) + G_c \, \mathcal{H}^2(\Gamma) \tag{6}$$

among all $(\mathbf{y}, \Gamma)$ with

$$\begin{cases} \mathbf{y}(\mathbf{X}) = \overline{\mathbf{y}}(\mathbf{X}, t_k), \quad \mathbf{X} \in \partial\Omega_0^{\mathcal{D}} \\ \mathbf{y}(\mathbf{X}) \text{ satisfies material impenetrability} \\ \Gamma \setminus \Gamma_{k-1} \subset \mathcal{V}_{\mathcal{F}}(t_{k-1}) \\ \Gamma \supset \Gamma_{k-1} \\ \Gamma \cap \{\text{a specified neighborhood of } \partial\Omega_0^{\mathcal{D}} \cup \text{ supp } \overline{\mathbf{s}}_k\} = \emptyset \end{cases} . \tag{7}$$

In these expressions, $\mathcal{H}^2(\Gamma)$ denotes, again, the 2-dimensional Hausdorff measure of the unknown crack Γ in the undeformed configuration and

$$\mathcal{V}_{\mathcal{F}}(t) = \{\mathbf{X} \in \Omega_0 \setminus \Gamma_{k-1} : \mathcal{F}(\mathbf{S}(\mathbf{X}, t)) \geq 0\} \tag{8}$$

is the set of all material points at which the strength surface $\mathcal{F}(\mathbf{S}) = 0$ of the material is exceeded at time t, referred to as the strength violation set.

Of course, at such a level of generality and without further specifying the form and regularity of the various ingredients that enter the minimization process, it is impossible to assert the existence of such a minimizing pair. In particular, if $\mathbf{b}_k$ and/or $\overline{\mathbf{s}}_k \not\equiv 0$ and if

$$\text{the infimum of (6) is } -\infty,$$

then one should be extremely cautious. This will be so for example if it is possible to sever Ω_0 into two pieces Ω_1, Ω_2 with a crack Γ with $\Omega_1 \cap \partial\Omega_0^{\mathcal{D}} = \emptyset$ and if the torsor

$$\left(\int_{\Omega_1} \mathbf{b}_k \, \mathrm{d}\mathbf{X} + \int_{\partial\Omega_1} \overline{\mathbf{s}}_k \mathrm{d}\mathcal{H}^2, \int_{\Omega_1} \mathbf{X} \wedge \mathbf{b}_k \, \mathrm{d}\mathbf{X} + \int_{\partial\Omega_1} \mathbf{X} \wedge \overline{\mathbf{s}}_k \, \mathrm{d}\mathcal{H}^2 \right) \not\equiv 0$$

because then, severing the piece Ω_1 and moving it by a rigid body deformation will decrease the potential energy at will, at least provided this does not contradict material impenetrability. As of now, we do not have an all encompassing view of that case, except in the 2D case without tractions or body forces. This will be the object of the next section.

Remark 3.1. *The unbreakable boundary.* The unbreakable neighborhood of $\partial\Omega_0^{\mathcal{D}} \cup \text{ supp } \overline{\mathbf{s}}_{k-1}$ is not a material characteristic, but rather the recognition that a loaded boundary, be it by imposing a deformation or applying a force, necessitates an ad hoc reinforcement which makes it more difficult to break than the rest of the sample. Modeling the corresponding attachments is not part and parcel of a cogent theory of brittle fracture and would require the import of additional ingredients (like adhesion or gripping) that are external contributions that we do not wish to address herein.

Remark 3.2. *Fracture irreversibility and frictionless crack contact.* The formulation (5)-(7) assumes that fracture is an irreversible process — precluding crack healing — and that contact between crack surfaces is frictionless. The former assumption is particularly well-suited to monotonic loading conditions. The latter may be called into question when dealing with problems with pre-existing cracks under large compressive and shear loads.

Remark 3.3. *A critical material length scale ℓ_c and an explicit upper bound.* Consider the special case when a body free of pre-existing cracks is under a state of spatially uniform stress, $\mathbf{S}(\mathbf{X}, t) = \overline{\mathbf{S}}(t)$, as the result of an affine deformation $\overline{\mathbf{y}}(\mathbf{X}, t) = \overline{\mathbf{F}}(t)\mathbf{X}$ applied over the entirety of its boundary ($\partial\Omega_0^{\mathcal{D}} = \partial\Omega_0$). According to the admissibility constraint $(7)_3$, no crack can nucleate until the time at which $\overline{\mathbf{S}}(t)$ reaches

the strength surface of the material. Denote by $t = t_{k-1}$ that time. Then, according to the Definition 1.1 of strength, a crack should nucleate at $t = t_k$. This implies that the minimizing energy for the configuration with the nucleated crack is less than or equal to the energy for the configuration without the crack at $t = t_k$, that is,

$$\mathcal{E}(\mathbf{y}_k, \Gamma_k) = \int_{\Omega_0 \setminus \Gamma} W(\nabla \mathbf{y}_k)\, \mathrm{d}\mathbf{X} + G_c\, \mathcal{H}^2(\Gamma_k) \leq \int_{\Omega_0} W(\overline{\mathbf{F}}(t_k))\, \mathrm{d}\mathbf{X} = |\Omega_0| W(\overline{\mathbf{F}}(t_k)). \tag{9}$$

This inequality unveils an important constraint: the domain Ω_0 occupied by the body cannot be arbitrarily small. Specifically, there exists a critical material length scale, ℓ_c, below which this inequality is violated. Physically, this means that at scales smaller than ℓ_c, the strength surface $\mathcal{F}(\mathbf{S}) = 0$ ceases to be a valid macroscopic material property. Although the computation of ℓ_c is generally intractable analytically, establishing an explicit upper bound, ℓ_{bound}, is straightforward. To this end, we first note that

$$\mathcal{E}(\mathbf{y}_k, \Gamma_k) \leq G_c \operatorname{Per}(\Omega_0),$$

where $\operatorname{Per}(\Omega_0)$ denotes the perimeter of the domain Ω_0. It follows that domains that satisfy the condition

$$\ell_c \leq \max_{\mathcal{G}(\mathbf{F})=0} \frac{G_c}{W(\mathbf{F})} =: \ell_{bound} \leq \frac{|\Omega_0|}{\operatorname{Per}(\Omega_0)}, \quad \text{where} \quad \mathcal{G}(\mathbf{F}) \equiv \mathcal{F}\left(\frac{\partial W}{\partial \mathbf{F}}(\mathbf{F})\right),$$

satisfy the condition (9). As an example, we note that for the silicate glass considered throughout this work, with the material properties listed in Table 1, the smallest elastic energy density at strength is attained at $\mathbf{S} = \operatorname{diag}(28\,\mathrm{MPa}, 26.5\,\mathrm{MPa}, 10.2\,\mathrm{MPa})$, yielding the bound $\ell_{bound} = 1.37$ mm.

Remark 3.4. *Connection with the variational formulation of Francfort and Marigo and the classical Griffith energy competition.* The proposed formulation (5)-(7) builds directly upon the variational framework of Francfort and Marigo (1998) by introducing two critical constraints. First and foremost, the fundamental constraint $(7)_3$ ensures that competing add-cracks lie entirely within the strength violation set (8). Second, the technical constraint $(7)_4$ dictates that fracture at boundary regions — when subjected to prescribed deformations and non-zero loads — requires explicit modeling of the relevant interfacial mechanics.

Additionally, in the limiting case where a large pre-existing crack undergoes stable infinitesimal growth in opening mode, the formulation (5)-(7) reduces identically to the classical Griffith criterion $G = G_c$, subject to the interpretation of G_c detailed in Subsection 1.1.3.

Remark 3.5. *Non-convexity and computational tractability.* The energy functional (6) is generically not convex, even if the elastic energy density W is taken to be convex. This is because the surface energy contribution is strictly monotonically increasing in Γ, while the potential energy is monotonically decreasing in Γ. While this non-convexity makes the minimization challenging, the admissibility constraint $(7)_3$ — which restricts competing add-crack to lie entirely within the strength violation set (8) — is expected to be restrictive enough to render the problem more computationally tractable.

Remark 3.6. *Frame indifference, material symmetry, and strength.* As an intrinsic macroscopic material property, strength has frame indifference and material symmetry properties. So, we will assume henceforth that the set $\mathcal{F}(\mathbf{S}(\mathbf{X}, t)) \leq 0$ is actually a closed star-shaped subset $\mathcal{K}$ of $\mathbb{R}^3$ containing $\mathbf{0}$, its center, in its interior, the boundary of which must be attained by the eigenvalues of the monotonically increasing in time and spatially constant stress tensor when a crack nucleates.

4. First mathematical results: The case of isotropic linear elastic brittle materials in 2D

In this section, we specialize the theory to the case of a 2D homogeneous isotropic linear elastic brittle material under pure displacement boundary conditions. We do so because we can be more mathematically precise in such a setting, both in terms of the proposed formulation and of the currently achievable results.

Notationwise, we will be using the standard notation of isotropic linear elasticity. In particular the Lamé coefficients, Λ and μ, and the Young's modulus and Poisson's ratio, E and ν, will be used. We recall

that, classically in a N-dimensional setting, $\mu > 0, N\Lambda + 2\mu > 0$, $E > 0$ and $\nu \in]-1, 1/2[$ if $N = 2$, $\nu \in]-1/(N-2), 1/2[$ if $N \geq 3$. Further $\Lambda = \nu(1+\nu)/(E(1-(N-1)\nu))$, $\mu = (1+\nu)/(2E)$, and

$$\Lambda(\operatorname{tr} \mathbf{E})^2 + 2\mu\, \mathbf{E} \cdot \mathbf{E} \geq \alpha |\mathbf{E}|^2 \text{ for some } \alpha > 0. \tag{10}$$

For this section, we consider a bounded, open, connected, Lipschitz domain $\Omega_0 := \Omega$ with boundary $\partial\Omega := \partial\Omega^{\mathcal{D}} \cup \partial\Omega^{\mathcal{N}} \cup \Delta$ where $\partial\Omega^{\mathcal{D}}$ and $\partial\Omega^{\mathcal{N}}$ are disjoint relatively open sets and the relative boundary Δ has 0 $\mathcal{H}^1$-measure. We also abandon requirement $(7)_5$ for simplicity and also because it is not present in the by now classical description of variational fracture evolution.

4.1. Length scale

We first revisit and expand Remark 3.3 in the particular context detailed above. Here, as in Section 2, $\overline{\mathbf{y}}(\mathbf{X}, t) = \mathbf{X} + \mathbf{u}(\mathbf{X}, t)$ where $\mathbf{u}$ is the displacement field. The elastic energy density W is a function of $\mathbf{E}(\mathbf{u}) := 1/2(\nabla\mathbf{u} + \nabla\mathbf{u}^T)$ and the first Piola-Kirchhoff stress tensor $\mathbf{S}$ identifies with the Cauchy stress tensor $\boldsymbol{\sigma}$.

Because $\boldsymbol{\sigma}$ is constant throughout Ω, the elasticity problem for any time t is

$$\begin{cases} \mathbf{u} = t\mathbf{e}\mathbf{X} \text{ on } \partial\Omega \\ \mathbf{e} = \dfrac{1}{E}((1+\nu)t\boldsymbol{\sigma} - \nu \operatorname{tr}(t\boldsymbol{\sigma})\mathfrak{i}) \text{ in } \Omega \\ \operatorname{Div}(t\boldsymbol{\sigma}) = \mathbf{0} \text{ in } \Omega \end{cases}, \tag{11}$$

where the fourth equation above is automatically satisfied because $\boldsymbol{\sigma}$ is constant and $\mathfrak{i}$ stands for the identity mapping on $\mathbb{R}^3$.[7] The potential energy associated with (11) is

$$\frac{1}{2}t^2\mathcal{L}^2(\Omega)\left(\frac{1+\nu}{E}\boldsymbol{\sigma}\cdot\boldsymbol{\sigma} - \frac{\nu}{E}(\operatorname{tr}\boldsymbol{\sigma})^2\right).$$

Then, whenever t is such that $t\boldsymbol{\sigma} \in \partial K$, say at $t := t_{\boldsymbol{\sigma}}$, it must be so that

$$\frac{1}{2}t_{\boldsymbol{\sigma}}^2\mathcal{L}^2(\Omega)\left(\frac{1+\nu}{E}\boldsymbol{\sigma}\cdot\boldsymbol{\sigma} - \frac{\nu}{E}(\operatorname{tr}\boldsymbol{\sigma})^2\right) \geq \frac{1}{2}\int_{\Omega\setminus\Gamma}\left(\frac{1+\nu}{E}\boldsymbol{\tau}\cdot\boldsymbol{\tau} - \frac{\nu}{E}(\operatorname{tr}\boldsymbol{\tau})^2\right)\mathrm{d}\mathbf{X} + G_c\mathcal{H}^1(\Gamma) \tag{12}$$

for some closed $\overline{\Omega} \supset \Gamma \neq \emptyset$, where $\boldsymbol{\tau}(\mathbf{X})$ is the stress field solution to

$$\begin{cases} \mathbf{u} = t_{\boldsymbol{\sigma}}\mathbf{e}\mathbf{X} \text{ on } \partial\Omega^{\mathcal{D}} \setminus \Gamma \\ \mathbf{E}(\mathbf{u})(\mathbf{X}) = \dfrac{1}{E}((1+\nu)\boldsymbol{\tau} - \nu\operatorname{tr}(\boldsymbol{\tau})\mathfrak{i}) \text{ in } \Omega\setminus\Gamma \\ \operatorname{Div}(\boldsymbol{\tau}) = \mathbf{0} \text{ in } \Omega\setminus\Gamma \end{cases}.$$

Now, in particular, it is sufficient to take $\Gamma = \partial\Omega$, provided that Ω has finite perimeter in which case we obtain as sufficient condition

$$\frac{1}{2}t_{\boldsymbol{\sigma}}^2\mathcal{L}^2(\Omega)\left(\frac{1+\nu}{E}\boldsymbol{\sigma}\cdot\boldsymbol{\sigma} - \frac{\nu}{E}(\operatorname{tr}\boldsymbol{\sigma})^2\right) \geq G_c\operatorname{Per}(\Omega). \tag{13}$$

Note that the isoperimetric inequality (e.g., Ambrosio et al., 2000, Theorem 3.46), namely that $\operatorname{Per}(\Omega) \geq \sqrt{4\pi}(\mathcal{L}^2(\Omega))^{\frac{1}{2}}$ does not add any useful information to (13). In any case, since we can span all of ∂K by

[7] Because of frame indifference and material symmetry, we do not need to add to the displacement field a linearized rigid body motion, that is a term of the form $\mathbf{A}\mathbf{X} + \mathbf{c}$ where $\mathbf{A}$ is an arbitrary skew-symmetric matrix and $\mathbf{c}$ an arbitrary vector.

varying $\boldsymbol{\sigma}$ we obtain, upon setting $\boldsymbol{\tau} := t_{\boldsymbol{\sigma}}\boldsymbol{\sigma}$ in (13), that, for a domain Ω with finite perimeter made up of that material to be admissible for at least one nucleation event, it suffices that

$$\frac{1}{2}\max_{\boldsymbol{\tau}\in\partial K}\left\{\frac{1+\nu}{E}\boldsymbol{\tau}\cdot\boldsymbol{\tau}-\frac{\nu}{E}(\mathrm{tr}\,\boldsymbol{\tau})^2\right\}\geq G_c\frac{\mathrm{Per}\,(\Omega)}{\mathcal{L}^2(\Omega)}. \tag{14}$$

Recalling Remark 3.6, we thus obtain from (14) that the following proposition holds true.

Proposition 4.1. *If the bounded open set Ω has finite perimeter, then a crack can nucleate in $\overline{\Omega}$ provided that*

$$\frac{\mathcal{L}^2(\Omega)}{\mathrm{Per}\,(\Omega)}\geq 2G_cE\min_{(\lambda_1,\lambda_2)\in\mathcal{K}}\frac{1}{(\lambda_1^2+\lambda_2^2)-2\nu\lambda_1\lambda_2}. \tag{15}$$

This proposition introduces a minimal length-scale for $\mathcal{L}^2(\Omega)/\mathrm{Per}\,(\Omega)$ which, if satisfied, will ensure that some kind of nucleation event can take place. In particular, it points to a notion of fatness of the domain. Indeed a very thin and long domain would generically violate (15), at least provided that the right hand-side is not 0.

Remark 4.2. Note that, by appealing to a result of Federer (e.g., Evans and Gariepy, 1992, Theorem 3.46, Section 5.11), any bounded set with Lipschitz boundary has finite perimeter. The same would hold true of a Lipschitz domain Ω with a (smooth) pre-crack Γ such that $\mathcal{H}^1(\Gamma\cap\partial\Omega)<\infty$.

Remark 4.3. *Difference with cohesive fracture.* The interested reader will remark that, in the setting of cohesive fracture, nucleation must occur when, in essence, the stress state reaches the slope at 0 of the surface energy (e.g., Bourdin et al., 2008, Section 4.2) and this at a single material point. There, nucleation is not connected to any kind of minimality, but only to a first order necessary condition for any kind of minimality, whereas here, global minimality plays a decisive role in obtaining (12).

Further, there is no intrinsic length-scale in the cohesive notion of strength. In other words the meaningful domains from the standpoint of fracture are not constrained by the strength. Our approach, to the contrary, imparts a length-scale which operates as a selection criterion for domains for which fracture can take place. This we view as both a positive and a distinguishing feature.

4.2. The discrete evolution

Let us now rewrite the constrained energy minimization problem put forth in Section 3 in the specific setting at hand and when no tractions or body forces are present.

As mentioned before, we are unable at this time to put forth a time-continuous evolution for an elastic brittle domain subjected to a quasi-static loading process. This is so because the nature of the dissipation carried by the strength eludes us. As was seen in Section 2, there might be a drop of energy when the crack experiences a sudden jump in length. That drop is not seen in the classical formulation (Francfort and Larsen, 2003; Dal Maso et al., 2005) where the only non-zero boundary conditions are on a Dirichlet part of the boundary.

We will take, for $t_0=0\leq t_1\leq\ldots\leq t_N=t$ the loading process to be of the form

$$\overline{\mathbf{u}}_k \text{ a } \mathbf{X}\text{-dependent imposed displacement on } \partial\Omega^{\mathcal{D}}$$

with adequate regularity (say C^1 for example).

The formulation is detailed below. It starts with the definition of the admissible test cracks and displacement fields.

Definition 4.4 (The admissible configurations). *We set all quantities with index -1 to be 0. Knowing $\Gamma_{k-1},\mathbf{u}_{k-1},\boldsymbol{\sigma}_{k-1}:=\Lambda\mathrm{Div}\,\mathbf{u}_{k-1}\mathbf{i}+2\mu\mathbf{E}(\mathbf{u}_{k-1})$ the stress field associated to $\mathbf{u}_{k-1}$, we define*

$$\Sigma_{k-1}:=\overline{\{\mathbf{X}\in\Omega\setminus\Gamma_{k-1}:\boldsymbol{\sigma}_{k-1}(\mathbf{X})\notin\mathring{\mathcal{K}}\}} \tag{16}$$

where $\mathcal{K}$ was defined in Remark 3.6.

We say that the pair $(\mathbf{u},\Gamma)$ *is an admissible configuration at time* t_k *for the boundary displacement* $\overline{\mathbf{u}}_k \in H^1(\Omega;\mathbb{R}^2)$ *if*

$$\Gamma \in \mathcal{K}^k_m(\overline{\Omega}) \text{ and } \mathbf{u} \in \mathscr{LD}(\Omega\setminus\Gamma) \text{ with } \mathbf{u} = \overline{\mathbf{u}}_k \text{ on } \partial\Omega^{\mathcal{D}}\setminus\Gamma,$$

where $m \geq 1$ *is a fixed number, where, for any open set* A,

$$\mathscr{LD}(A) := \{\mathbf{v} \in L^2_{loc}(A;\mathbb{R}^2) : \mathbf{E}(\mathbf{u}) \in L^2(A;\mathbb{R}^{2\times 2})\}$$

and where

$$\mathcal{K}^k_m(\overline{\Omega}) := \{\Gamma \text{ closed subset of } \bar{\Omega} \text{ with at most } m \text{ connected components,}$$
$$\Gamma_{k-1} \subset \Gamma \subset \Gamma_{k-1}\cup\Sigma_{k-1} \text{ and } \mathcal{H}^1(\Gamma) < +\infty\}.$$

We will write $(\mathbf{u},\Gamma) \in \mathcal{A}(\overline{\mathbf{u}}_k)$. *The pair* $(\mathbf{u},\mathbf{E}(\mathbf{u}))$ *can be thought of as an element of* $L^2_{loc}(\Omega;\mathbb{R}^2)\times L^2(\Omega;\mathrm{M}^2_{\mathrm{sym}})$ *since* Γ *has null Lebesgue measure.*

The family of closed sets in $\mathbb{R}^N$ can be endowed with the Hausdorff metric d_H defined by

$$d_H(K_1,K_2) := \max\left\{\sup_{x\in K_1}\operatorname{dist}(x,K_2), \sup_{y\in K_2}\operatorname{dist}(y,K_1)\right\}$$

with the conventions $\operatorname{dist}(x,\emptyset) = +\infty$ and $\sup\emptyset = 0$, so that $d_H(\emptyset,K) = 0$ if $K = \emptyset$ and $d_H(\emptyset,K) = +\infty$ if $K \neq \emptyset$. The Hausdorff metric has good compactness properties (e.g., Ambrosio and Tilli, 2004, Theorem 4.4.15).

Proposition 4.5 (Compactness). *Let* $(\Gamma_n)_{n\in\mathbb{N}}$ *be a sequence of compact sets contained in a fixed compact set* C *of* $\mathbb{R}^N$. *Then there exists a compact set* $\Gamma \subseteq C$ *such that up to a subsequence*

$$\Gamma_n \to \Gamma \qquad \text{in the Hausdorff metric.}$$

Then the formulation hinges on the following minimization scheme.

Definition 4.6 (The minimization scheme). *Compute*

$$\mathcal{I} := \inf_{(\mathbf{u},\Gamma)} \int_{\Omega\setminus\Gamma} \frac{1}{2}\left(\Lambda(\operatorname{Div}\mathbf{u}(\mathbf{X}))^2 + 2\mu\mathbf{E}(\mathbf{u}(\mathbf{X}))\cdot\mathbf{E}(\mathbf{u}(\mathbf{X}))\right)\mathrm{d}\mathbf{X} + G_c\mathcal{H}^1(\Gamma)$$

over all pairs $(\mathbf{u},\Gamma) \in \mathcal{A}(\overline{\mathbf{u}}_k)$. *Denote by* $(\mathbf{u}_{k+1},\Gamma_{k+1})$ *a minimizer.*

If we restrict the setting to cracks that are closed sets with a uniformly bounded number of connected components, say m, then the incremental problem is well-posed. Indeed, consider a minimizing sequence $(\mathbf{u}_n,\Gamma_n)$. Since $\Gamma_{k-1}\cup\Sigma_{k-1}$ with Σ_{k-1} defined in (16) is a compact set we can apply Proposition 4.5 to Γ_n and we obtain that, up to a subsequence (not relabeled), Γ_n Hausdorff converges to $\Gamma \in \mathcal{K}^k_m(\overline{\Omega})$. Further, in view of (10), we can also assume that $\mathbf{E}(\mathbf{u}_n)$ converges weakly in $L^2(\Omega;\mathrm{M}^N_{\mathrm{sym}})$ to some Φ.

With this the following compactness result (Francfort et al., 2019, Lemma 5.2) applies to the setting at hand.

Lemma 4.7. *Let* $\overline{\mathbf{u}}_n, \overline{\mathbf{u}} \in H^1(\Omega;\mathbb{R}^2)$ *be such that*

$$\overline{\mathbf{u}}_n \to \overline{\mathbf{u}} \qquad \text{strongly in } H^1(\Omega;\mathbb{R}^2).$$

Assume that $(\mathbf{u}_n,\Gamma_n) \in \mathcal{A}(\overline{\mathbf{u}}_n)$ *with*

$$\mathbf{E}(\mathbf{u}_n) \rightharpoonup \Phi \qquad \text{weakly in } L^2(\Omega;\mathrm{M}^N_{\mathrm{sym}}),$$

and

$$\Gamma_n \to \Gamma \qquad \text{in the Hausdorff metric.}$$

Then there exists $(\mathbf{u},\Gamma) \in \mathcal{A}(\overline{\mathbf{u}})$ *such that* $\Phi = \mathbf{E}(\mathbf{u})$ *on* $\Omega\setminus\Gamma$.

It now suffices to apply Gołąb's theorem (e.g., Ambrosio and Tilli, 2004, Theorem 4.4.17).

Theorem 4.8 (Gołąb's). *Let $(K_n)_{n\in\mathbb{N}}$ be a sequence of compact connected sets in $\mathbb{R}^N$ such that*

$$K_n \to K \qquad \text{in the Hausdorff metric.}$$

Then K is connected and for every open set $A \subseteq \mathbb{R}^N$

$$\mathcal{H}^1(K \cap A) \leq \liminf_{n\to\infty} \mathcal{H}^1(K_n \cap A).$$

Note that the lower semicontinuity in Gołąb's Theorem still holds when K_n has a uniformly bounded number of connected components. The conclusion is reached thanks to Lemma 4.7, to Gołąb's Theorem and to obvious arguments of weak lower-semicontinuity.

Remark 4.9. In the case where either non-zero traction forces and/or non-zero body forces are present, the situation is more complex and several issues may arise: the lack of bounds on the crack length of the minimizing sequences, the lack of L^1 regularity of the test displacement fields, etc. This may occur whether the infimum of (6) is finite or not. In particular, the crack may sever Ω into pieces that — non-interpenetrability permitting — can be moved to infinity as rigid bodies, generically producing an infimum equal to $-\infty$ as mentioned earlier in Section 3. This will be the object of our next contribution.

5. Compliance with *"The Nine Circles of Elastic Brittle Fracture"* on glass and rubber

In a recent contribution, Kamarei et al. (2026b) introduced "The Nine Circles of Elastic Brittle Fracture," a comprehensive obstacle course of nine challenge problems designed to assess the viability of any proposed fracture theory. As defining features, these problems can be carried out experimentally with standard testing equipment and, more critically, span the full spectrum of well-established experimental knowledge for both fracture nucleation and propagation. Specifically, they examine nucleation dominated by material strength under uniform stress, by the Griffith energy competition from large pre-existing cracks, and by the more complex interplay between strength and Griffith energy competition under non-uniform stress states, be they singular or not. For propagation, the problems examine crack growth under opening (Mode I) and tearing (Mode III) conditions. Failure to accurately resolve even a single "circle" disqualifies a theory as a viable framework for describing, and hence predicting, fracture in general.

In this section we subject the proposed theory (5)-(7) to "The Nine Circles of Elastic Brittle Fracture." Two circles have already been successfully tested. Section 2 addresses the 1$^{\text{st}}$ circle (nucleation under uniaxial tension), and in (Lopez-Pamies and Kamarei, 2025), it was tested against the 4$^{\text{th}}$ circle (nucleation from a large pre-existing crack under opening mode). In that study, the theory was also directly compared with classical experiments on nucleation from large pre-existing cracks under complex loading conditions to validate its predictions of non-trivial crack paths. Consequently, we focus here on the seven remaining challenge problems. Much like in (Kamarei et al., 2026b), the results pertain to the same hard silicate glass investigated in Section 2, as well as to a soft synthetic rubber with Neo-Hookean elastic energy density

$$W(\mathbf{F}) = \frac{\mu}{2}\,(I_1 - 3) - \mu \ln J + \frac{\Lambda}{2}(J-1)^2,$$

Table 3: Material constants for the synthetic rubber used throughout this work.

Elasticity constants	μ (MPa)	Λ (MPa)
	0.52	85.77
Strength constants	$s_{\texttt{ts}}$ (MPa)	$s_{\texttt{hs}}$ (MPa)
	0.3	1
Fracture toughness	G_c (N/m)	
	41	

Drucker-Prager strength surface (2), scalar critical energy release rate G_c, and the material constants listed in Table 3; note that in terms of the hydrostatic strength, $s_{\mathtt{hs}}$, the uniaxial compressive strength is given by $s_{\mathtt{cs}} = 3s_{\mathtt{hs}}s_{\mathtt{ts}}/(3s_{\mathtt{hs}} - 2s_{\mathtt{ts}})$. Specifically, the poker-chip (7^{th} circle) and trousers (9^{th} circle) tests are carried out on the synthetic rubber, whereas the remaining five are conducted on the silicate glass.

5.1. Biaxial tension test

We begin by considering the 2^{nd} circle, a circular plate of radius $R = 5$ mm and thickness $B = 0.25$ mm that is subjected to equi-biaxial tension via a uniform radial displacement u applied at its lateral boundary $\mathbf{X} \in \partial\Omega_l = \{\mathbf{X} : X_1^2 + X_2^2 = R^2,\ -B/2 < X_3 < B/2\}$, while its top and bottom boundaries remain traction-free. Here, $\{\mathbf{e}_1, \mathbf{e}_2, \mathbf{e}_3\}$ stands for the laboratory frame indicated in the test schematic shown in Fig. 11(a). This boundary condition generates a spatially uniform biaxial strain, u/R, and a corresponding uniform biaxial stress, S, within the plate. Precisely,

$$\mathbf{E} = \frac{u}{R}(\mathbf{e}_1 \otimes \mathbf{e}_1 + \mathbf{e}_2 \otimes \mathbf{e}_2) + e_t \mathbf{e}_3 \otimes \mathbf{e}_3 \quad \text{and} \quad \mathbf{S} = S(\mathbf{e}_1 \otimes \mathbf{e}_1 + \mathbf{e}_2 \otimes \mathbf{e}_2),$$

where e_t denotes the transverse strain induced by the Poisson effect. This uniform state of stress and strain persists until the stress S reaches the material's biaxial tensile strength $s_{\mathtt{bs}}$; for the silicate glass of interest in this work, $s_{\mathtt{bs}} = 2s_{\mathtt{ts}}s_{\mathtt{cs}}/(3s_{\mathtt{cs}} - 2s_{\mathtt{ts}}) = 27$ MPa. At this critical threshold, a through-thickness crack abruptly nucleates and rapidly propagates, severing the plate into multiple fragments. Due to the inherent spatial variations in strength, the exact location of crack nucleation is inherently arbitrary.

As in Section 2, we deploy the proposed theory (5)-(7) by first numerically determining the strain u/R at which the strength condition $\mathcal{F}(\mathbf{S}) \geq 0$ is initially satisfied within some region of the plate. For definiteness, we consider the presence of a weaker central circular region with a 4 mm diameter where the uniaxial tensile strength is 10% lower ($s_{\mathtt{ts}} = 40$ MPa) than the surrounding material ($s_{\mathtt{ts}} = 44$ MPa). The strength condition $\mathcal{F}(\mathbf{S}) \geq 0$ is first satisfied in such a weaker region at $u/R = 3.0 \times 10^{-4}$. At this strain, we then numerically determine the energy (6) for plates containing straight through-thickness test cracks, $\Gamma = \Gamma(A)$, of crack length A, so that $\mathcal{H}^2(\Gamma) = AB$; see Fig. 11(b). Due to loading symmetry and material isotropy, different crack orientations need not be considered. Figure 11(c) presents the resulting energy $\mathcal{E}$ as a function of A assuming plane-stress conditions. The main observation from this figure is that the crack of length $A = 4$ mm — the largest possible length that can be fitted within the strength violation region — minimizes the energy $\mathcal{E}$. According to the theory (5)-(7), this implies that such a crack nucleates at $u/R = 3.0 \times 10^{-4}$, consistent with the reference result. It is also worth noting that no crack nucleates — because the energy

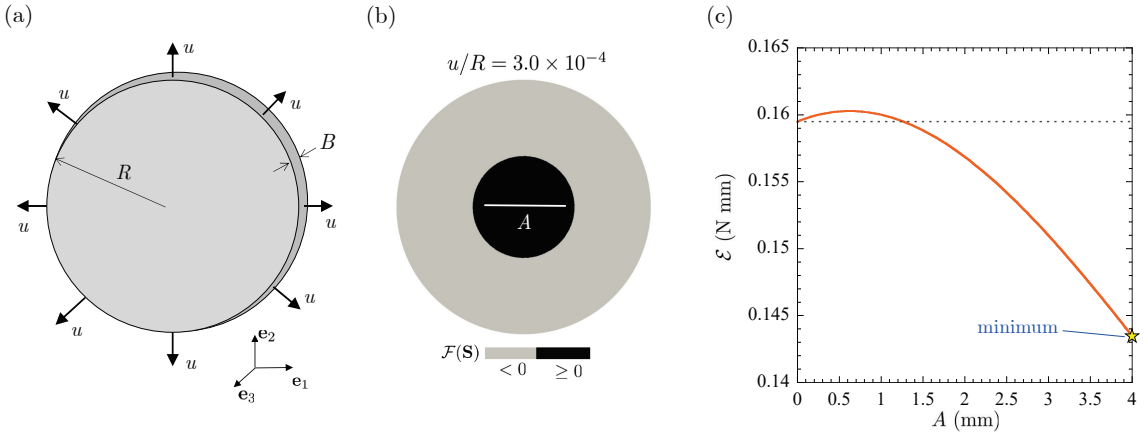


Figure 11: (a) Schematic of the biaxial tension test on silicate glass. (b) Contour plot of the region of the specimen where the stress field first exceeds ($\mathcal{F}(\mathbf{S}) \geq 0$) the strength surface of the material, depicting the test cracks considered within, at $u/R = 3.0 \times 10^{-4}$. (c) The corresponding energy $\mathcal{E}$ of the specimen plotted as a function of the test crack length A.

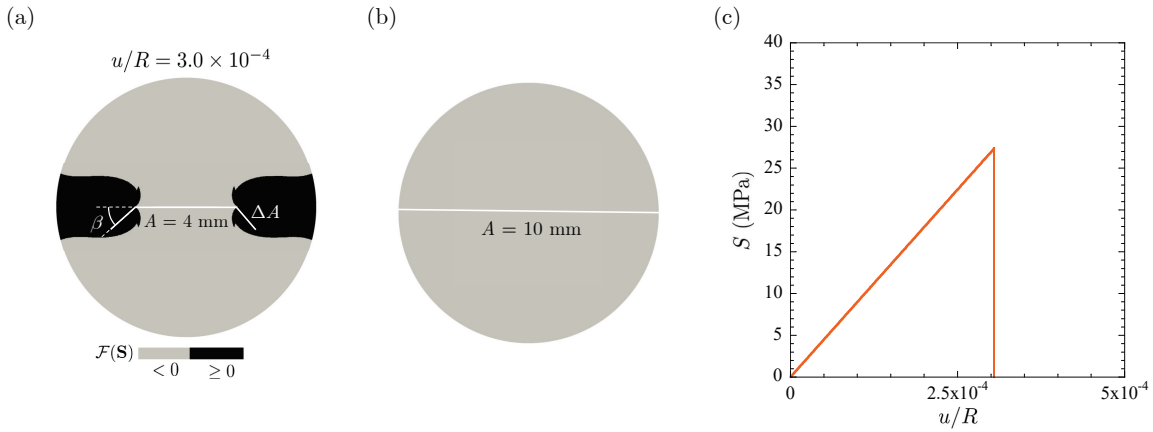


Figure 12: (a) The specimen at the applied strain $u/L = 3.0\times10^{-4}$ containing the initial minimizing crack ($A = 4\,\text{mm}$), depicting the regions where the stress field exceeds ($\mathcal{F}(\mathbf{S}) \geq 0$) the strength surface of the material along with the test add-cracks of length ΔA oriented at angles β considered within. (b) Schematic of the severed state of the specimen following the brutal propagation of the crack at $\beta = 0^\circ$ dictated by the theory. (c) The global stress S as a function of the applied strain u/R predicted by the theory.

is minimized by $A = 0$ — if the strength violation is confined to an area with a diameter under $\ell_{\texttt{bs}} = 1.25$ mm. This defines the length scale below which the biaxial tensile strength $s_{\texttt{bs}}$ can no longer be taken as a macroscopic material property; see Remark 3.3.

We now examine the minimizing solution with crack length $A = 4$ mm. At the critical applied strain of $u/R = 3.0 \times 10^{-4}$, we numerically identify the regions where the stress field violates the strength surface, $\mathcal{F}(\mathbf{S}) \geq 0$. As the contour plot in Fig. 12(a) illustrates, this strength violation is localized near the crack fronts. Within these specific regions, we introduce straight through-thickness test add-cracks. These are characterized by an added length ΔA — yielding a total crack surface of $\mathcal{H}^2(\Gamma) = (A + 2\Delta A)B$ — and an orientation β relative to the initial crack, as depicted schematically in Fig. 12(a). Our results indicate that the energy $\mathcal{E}$ is minimized at $\Delta A = 3\,\text{mm}$ and $\beta = 0^\circ$. That is, the proposed constrained minimization dictates that the nucleated crack at $u/R = 3.0\times10^{-4}$ does *not* stay put, instead it propagates by a finite-size growth in the same initial crack direction severing the specimen. Figures 12(b) and (c) display the resulting severed configuration and the complete global stress-strain response predicted by the theory, both of which align with the reference result.

5.2. Torsion test

We now consider the 3$^{\text{rd}}$ circle, a thin-walled circular tube with an initial length $L = 5$ mm, an inner radius $R_i = 2.85$ mm, and an outer radius $R_o = 3$ mm. The tube is subjected to torsion via an angle of twist ϕ applied at one end, while the opposite end remains rigidly fixed; see Fig. 13(a). Under these conditions, the tube experiences a state of shear strain and shear stress of the form

$$\mathbf{E} = \frac{\phi X_1}{2L}(\mathbf{e}_2 \otimes \mathbf{e}_3 + \mathbf{e}_3 \otimes \mathbf{e}_2) - \frac{\phi X_2}{2L}(\mathbf{e}_1 \otimes \mathbf{e}_3 + \mathbf{e}_3 \otimes \mathbf{e}_1) = \gamma(\mathbf{e}_\Theta \otimes \mathbf{e}_Z + \mathbf{e}_Z \otimes \mathbf{e}_\Theta) \tag{17}$$

and

$$\mathbf{S} = \frac{2TX_1}{\pi(R_o^4 - R_i^4)}(\mathbf{e}_2 \otimes \mathbf{e}_3 + \mathbf{e}_3 \otimes \mathbf{e}_2) - \frac{2TX_2}{\pi(R_o^4 - R_i^4)}(\mathbf{e}_1 \otimes \mathbf{e}_3 + \mathbf{e}_3 \otimes \mathbf{e}_1) = \tau(\mathbf{e}_\Theta \otimes \mathbf{e}_Z + \mathbf{e}_Z \otimes \mathbf{e}_\Theta) \tag{18}$$

for $\mathbf{X} \in \Omega = \{\mathbf{X} : R_i^2 < R^2 < R_o^2,\, 0 < X_3 < L\}$ with $R = \sqrt{X_1^2 + X_2^2}$. Here, $\{\mathbf{e}_1, \mathbf{e}_2, \mathbf{e}_3\}$ is the laboratory frame depicted in the figure, whereas $\{\mathbf{e}_R, \mathbf{e}_\Theta, \mathbf{e}_Z\}$ denotes the associated cylindrical frame of reference, $\gamma = \phi R/(2L)$ is the shear strain, T denotes the resultant torque at the tube ends, and $\tau = 2TR/(\pi(R_o^4 - R_i^4))$ stands for the corresponding shear stress.

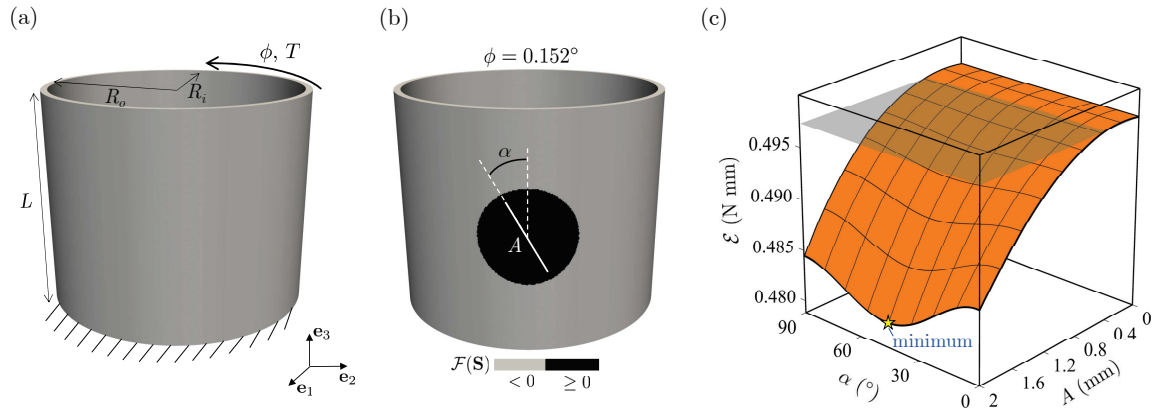


Figure 13: (a) Schematic of the torsion test on silicate glass. (b) Contour plot of the region of the specimen where the stress field first exceeds ($\mathcal{F}(\mathbf{S}) \geq 0$) the strength surface of the material, depicting the test cracks considered within, at $\phi = 0.152°$. (c) The corresponding energy $\mathcal{E}$ of the specimen plotted as a function of the test crack outer arc length A and angle α.

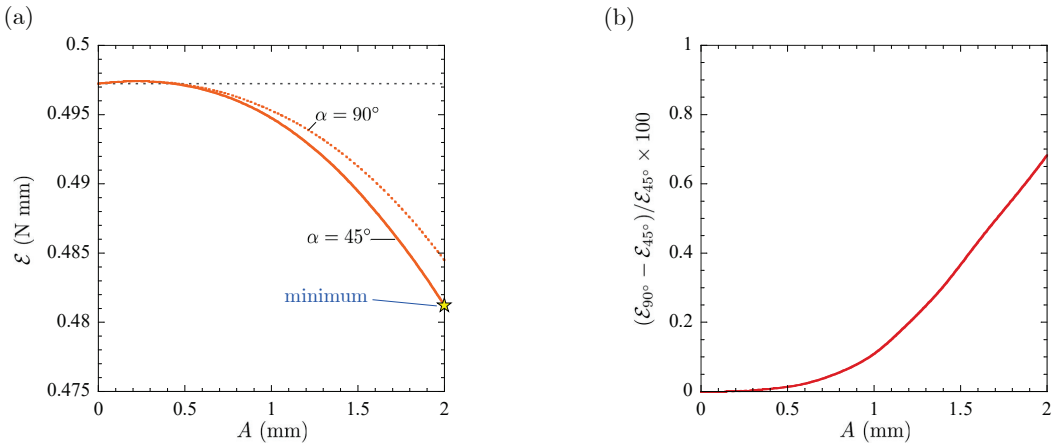


Figure 14: (a) The variation of the energy $\mathcal{E}$ as a function of crack length A for fixed crack angles $\alpha = 45°$ and $90°$. (b) The corresponding percentage difference in $\mathcal{E}$ between the two cases.

Because the tube is thin ($t = R_o - R_i = 0.15$ mm relative to $R_o = 3$ mm), the stress (18) and strain (17) fields are nearly uniform, with average values of $S = T(R_i + R_o)/(\pi(R_o^4 - R_i^4)) = T(R_i - t)/(2\pi R_i^3 t) + O(t)$ and $\phi(R_i + R_o)/(4L) = \phi(2R_i + t)/(4L)$. This quasi-uniform state persists until the macroscopic shear stress S reaches the material's shear strength $s_{\mathtt{ss}}$; for the silicate glass of interest in this work, $s_{\mathtt{ss}} = 2s_{\mathtt{ts}}s_{\mathtt{cs}}/(\sqrt{3}(s_{\mathtt{cs}} + s_{\mathtt{ts}})) = 44.4$ MPa. At this threshold, abrupt cracking severs the tube. While material stochasticity causes these cracks to form at arbitrary locations, experimentally they consistently exhibit a 45° orientation relative to the symmetry axis $\mathbf{e}_3$ — an orientation classically attributed to maximum principal stress alignment; see, e.g., Chapter 3 in the popular textbook Beer et al. (2019) and Remark 5.1.

As with the previous cases, we start by determining the angle of twist ϕ at which the strength condition $\mathcal{F}(\mathbf{S}) \geq 0$ is first satisfied within some region of the tube. For definiteness, we consider the presence of a weaker through-thickness cylindrical region with a 2 mm diameter where the uniaxial tensile strength is 10% lower ($s_{\mathtt{ts}} = 40$ MPa) than the surrounding material ($s_{\mathtt{ts}} = 44$ MPa). The strength criterion $\mathcal{F}(\mathbf{S}) \geq 0$ is initially met in this weaker region at $\phi = 0.152°$. At this critical angle of twist, we numerically determine the energy (6) for tubes containing straight through-thickness test cracks of outer arc length A, inner arc length AR_i/R_o, and thickness $t = R_o - R_i$ — yielding a crack surface area of $\mathcal{H}^2(\Gamma) = At(2R_i + t)/(2(R_i + t)) =$

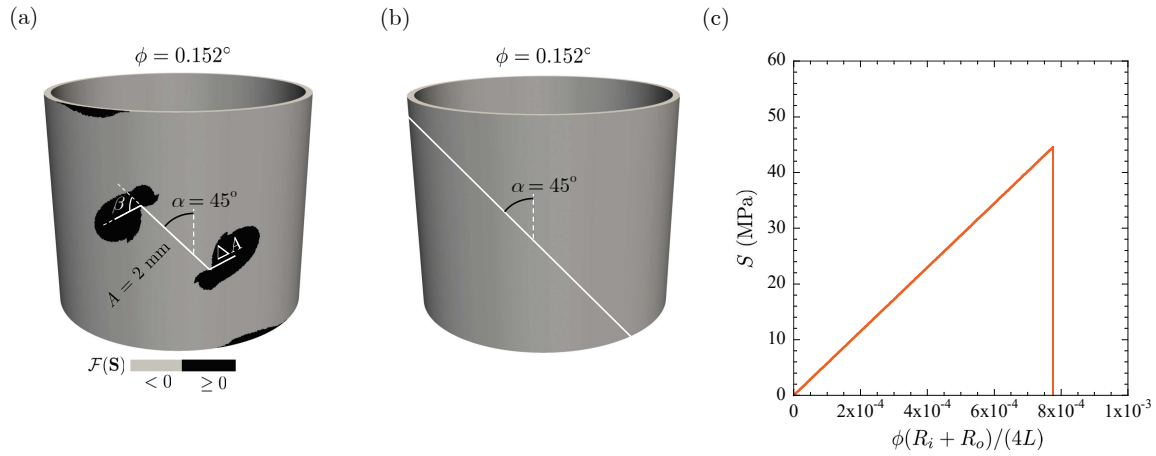


Figure 15: (a) The specimen at the critical applied angle of twist $\phi = 0.152°$ containing the initial minimizing crack ($A = 2\,\text{mm}, \alpha = 45°$), depicting the regions where the stress field exceeds ($\mathcal{F}(\mathbf{S}) \geq 0$) the strength surface of the material along with the test add-cracks of length ΔA oriented at angles β considered within. (b) Schematic of the severed state of the specimen following the brutal propagation of the crack at $\beta = 0°$ dictated by the theory. (c) The global stress S as a function of the global strain $\phi(R_i + R_o)/(4L)$ predicted by the theory.

$At + O(t^2)$ — and an orientation α relative to the symmetry axis of the tube; see Fig. 13(b). Figure 13(c) presents the resulting energy $\mathcal{E}$ as a function of A and α. To visualize the quantitative aspects of the results more clearly, Fig. 14(a) plots $\mathcal{E}$ as a function of A for fixed orientations $\alpha = 45°$ and $90°$, while Fig. 14(b) plots the percentage difference in $\mathcal{E}$ between these two cases.

Figures 13(c) and 14 suggest the following. First and foremost, the energy $\mathcal{E}$ is minimized by a crack with an outer arc length $A = 2$ mm — the largest crack that can be accommodated within the strength-violation region — oriented at $\alpha = 45°$. According to the theory (5)-(7), this indicates that a crack nucleates at an angle of twist of $\phi = 0.152°$ along this orientation, in agreement with the reference result. Second, if the strength violation is restricted to a region with a diameter smaller than $\ell_{\text{ss}} = 0.44$ mm, the energy minimum shifts to $A = 0$, meaning no crack nucleates. As detailed in Remark 3.3, this establishes the critical length scale below which the shear strength s_{ss} ceases to be treatable as a macroscopic material property.

We next examine the minimizing solution with crack length $A = 2$ mm oriented at $\alpha = 45°$. At the critical applied angle of twist $\phi = 0.152°$, we numerically identify the regions where the stress field violates the strength surface, $\mathcal{F}(\mathbf{S}) \geq 0$. As illustrated by the contour plot in Fig. 15(a), this strength violation is localized near the crack fronts, as well as around small regions on the top and bottom boundaries. Within the former, we consider straight through-thickness test add-cracks defined by an additional outer arc length ΔA and an orientation angle β relative to the initial crack direction, yielding a total crack surface area of $\mathcal{H}^2(\Gamma) = (A + 2\Delta A)t(2R_i + t)/(2(R_i + t)) = (A + 2\Delta A)t + O(t^2)$. Our computations show that the energy $\mathcal{E}$ is minimized at $\Delta A = 0.31$ mm and $\beta = 0°$. This implies that the crack nucleated at $\phi = 0.152°$ does not remain stationary, but instead undergoes finite-size growth along its original trajectory. Subsequent computations reveal that the crack continues to propagate along this path until the tube is severed. Figures 15(b) and (c) display the resulting fractured configuration and the predicted global stress-strain response, both of which are in agreement with the reference results.

Remark 5.1. The proposed theory demonstrates that in elastic brittle tubes subjected to torsion, cracks nucleate and propagate at a 45° angle because this trajectory minimizes the energy (6). In this particular setting, the energy-minimizing direction coincidentally aligns with the plane orthogonal to the maximum principal stress. Because of this, it has become a mantra that orthogonality to the maximum principal stress direction is the physical explanation for the observed fracture angle (e.g., Beer et al., 2019). However the maximum principal stress criterion does not agree with many other experimental observations.

5.3. Single edge notch test

In contrast to the previous circles which considered fracture nucleation under spatially (quasi-)uniform stress states, this subsection and the subsequent two subsections shift focus to the 5^{th} through 7^{th} circles, which examine fracture nucleation under spatially non-uniform stress fields.

We proceed with the 5^{th} circle, the single edge notch test depicted in Fig. 16(a). The specimens consist of thin strips with a length $L = 25$ mm, width $H = 5$ mm, and thickness $B = 0.25$ mm. Each specimen features a pre-existing, through-thickness edge crack of various lengths $A = 0.025, 0.1, 0.5, 1$, and 1.5 mm. The specimens are rigidly clamped along their top and bottom boundaries and pulled apart by a prescribed global displacement u, generating a resultant reaction force P. We denote the corresponding nominal global stress by $S = P/(BH)$. As the applied displacement u increases, the specimens respond elastically until reaching a critical threshold u_{cr}, at which point the pre-existing crack grows straight ahead. For silicate glass, the critical global stress at the onset of this fracture nucleation event, denoted by S_{cr}, is bounded from above as follows, according to (Kamarei et al., 2026b),

$$S_{cr} \leq \min\{s_{\mathtt{ts}}, S_G\} \quad \text{with} \quad S_G = \frac{\cos\left(\dfrac{\pi A}{2H}\right)\sqrt{\dfrac{G_c E}{\pi A}}}{\left(0.752 + 1.0431\dfrac{A}{H} + 0.6076\left(1 - \sin\left(\dfrac{\pi A}{2H}\right)\right)^3\right)\sqrt{\dfrac{2H}{\pi A}\tan\left(\dfrac{\pi A}{2H}\right)}}. \tag{19}$$

In particular, the equality $S_{cr} = S_G$ is approached for sufficiently large cracks, while $S_{cr} = s_{\mathtt{ts}}$ is approached for sufficiently small cracks.

Once again, we incrementally increase the displacement u to numerically identify the regions where the strength surface is violated, $\mathcal{F}(\mathbf{S}) \geq 0$. Such regions are invariably localized around the front of the pre-existing crack, as well as around the corners at the grips. At each increment, we determine the length ΔA of a straight through-thickness add-crack — with add-crack surface area of $\mathcal{H}^2(\Gamma) = \Delta A B$ — emanating from the pre-existing crack front that minimizes the energy (6). We consider only test add-cracks aligned with the pre-existing cracks and with straight fronts through the thickness, having previously checked that

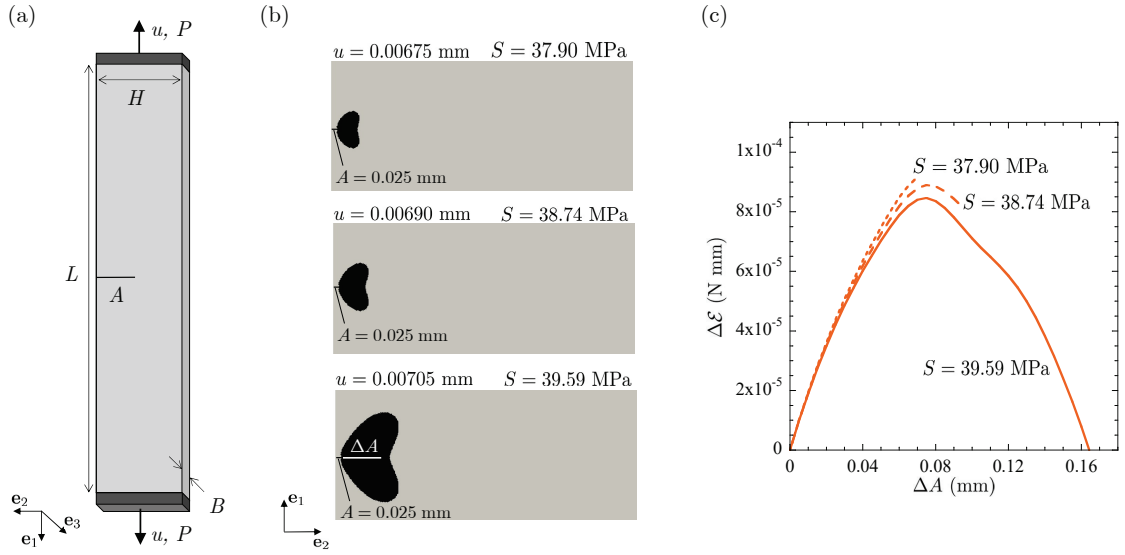


Figure 16: (a) Schematic of the single edge notch test on silicate glass. (b) Contour plots of magnified regions where the strength surface is violated ($\mathcal{F}(\mathbf{S}) \geq 0$) for a specimen with a pre-existing crack of length $A = 0.025$ mm, illustrating the considered test add-cracks, at three applied displacements u and global stresses $S = P/(BH)$. (c) The corresponding energy difference $\Delta\mathcal{E} = \mathcal{E} - \mathcal{E}|_{\Delta A=0}$ plotted as a function of the add-crack length ΔA.

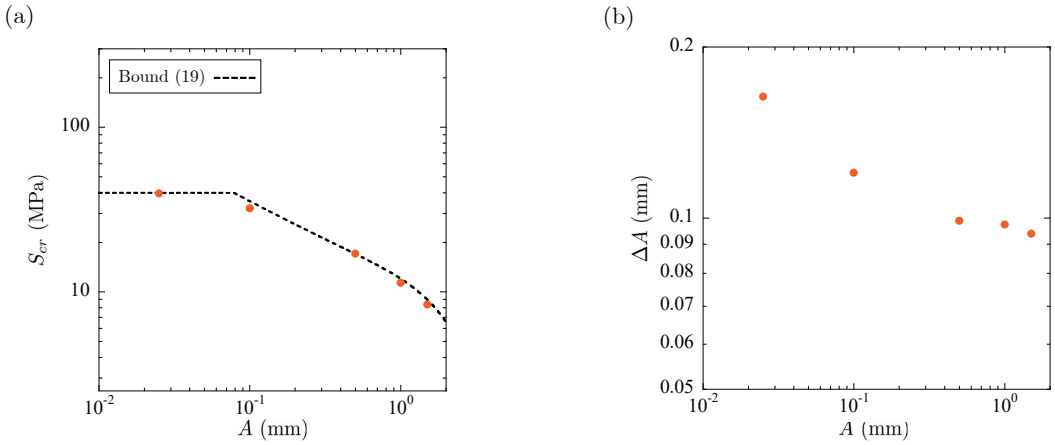


Figure 17: (a) The critical global stress S_{cr} and (b) the associated add-crack length ΔA as a function of the pre-existing crack length A, as predicted by the theory.

neither misaligned trajectories nor cracks nucleating from the corners yield energy minimizers, and that curved crack fronts have a minor effect on $\mathcal{E}$ due to the small specimen thickness ($B = 0.25$ mm).

Figures 16(b) and (c) present three representative results for the case of the smallest pre-existing crack, $A = 0.025$ mm. Specifically, Fig. 16(b) shows three magnified contour plots of the strength violation set at the applied displacements $u = 0.00675$ mm, 0.00690 mm, and 0.00705 mm — which correspond to global stresses $S = 37.90$ MPa, 38.74 MPa, and 39.59 MPa — depicting the add-cracks considered. Fig. 16(c) plots the corresponding energy $\mathcal{E}$ as a function of ΔA. More specifically, for better visualization, the figure plots the difference $\Delta\mathcal{E} = \mathcal{E} - \mathcal{E}|_{\Delta A=0}$ between the energy with the add-crack and the corresponding energy without it ($\Delta A = 0$). The results show that the pre-existing crack starts to grow when $u = u_{cr} = 0.00705$ mm at a global stress of $S_{cr} = 39.59$ MPa, consistent with the result (19). The crack growth is of finite length $\Delta A = 0.16351$ mm.

Figure 17 compiles the theoretical predictions for the critical global stress S_{cr} and the associated add-crack length ΔA for all five pre-existing crack lengths A. The main observation is that the theoretical predictions are once again in agreement with the reference result. It is also worth remarking that the length ΔA of the add-crack decreases monotonically with increasing A.

5.4. Indentation test of a block with a flat-ended cylindrical punch

Figure 18(a) shows a schematic of the 6$^{\text{th}}$ circle, a cylindrical block of height $L = 25$ mm and radius $R_b = 25$ mm, whose bottom boundary is firmly bonded to a rigid substrate. The block is frictionlessly indented along its axis of symmetry by a rigid, flat-ended cylindrical punch of radius $R_i = 1$ mm subjected to a prescribed displacement u. For silicate glass, the block initially deforms elastically. Upon reaching a critical displacement u_{cr}, a shallow ring crack nucleates from the surface of the specimen just outside the perimeter of the indenter ($R > R_i$). Further loading causes the crack to propagate at a roughly constant angle with respect to the surface, evolving into a cone (frustum) crack.

Once again, we incrementally increase the displacement u to numerically identify regions where the strength surface is violated, $\mathcal{F}(\mathbf{S}) \geq 0$. These regions emanate from the top surface of the specimen, adjacent to the indenter. Within these regions, for each displacement increment, we compute the energy (6) for specimens containing axisymmetric ring test cracks. These cracks have a depth A at a radial distance R from the symmetry axis, yielding a crack surface area of $\mathcal{H}^2(\Gamma) = 2\pi RA$; see Fig. 18(b). Figure 18(c) plots the resulting energy $\mathcal{E}$ as a function of A and R at $u = u_{cr} = 0.0160$ mm, the critical displacement at which a cracked configuration first minimizes (6). The results show that a ring crack of length $A = 0.0810$ mm at the distance $R = 1.4311$ mm from the symmetry axis minimizes the energy $\mathcal{E}$ at $u = u_{cr} = 0.0160$ mm. This is consistent with the reference result.

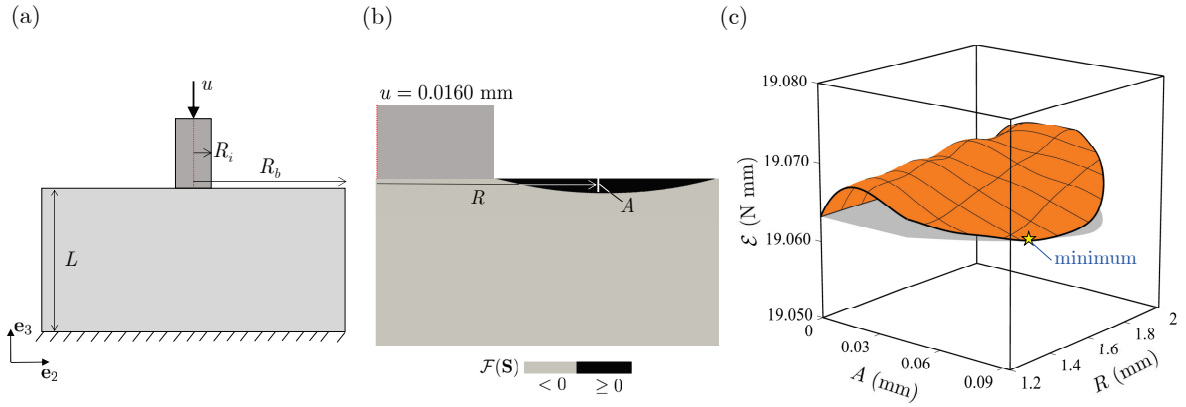


Figure 18: (a) Schematic of the indentation test on silicate glass. (b) Contour plot of a magnified region of the specimen where the stress field exceeds the strength surface of the material ($\mathcal{F}(\mathbf{S}) \geq 0$). The plot depicts the test cracks considered within this region and corresponds to $u = u_{cr} = 0.0160$ mm, the critical applied displacement at which a cracked configuration first minimizes the energy $\mathcal{E}$. (c) The corresponding energy $\mathcal{E}$ of the specimen plotted as a function of the test crack distance R from the symmetry axis and depth A.

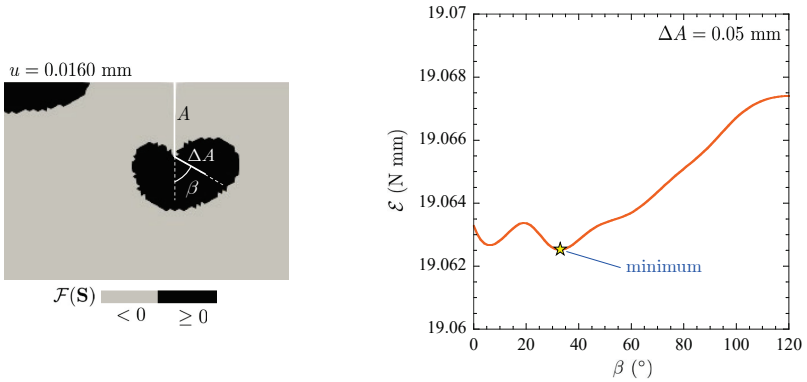


Figure 19: The specimen at the critical applied displacement $u = u_{cr} = 0.0160$ mm containing the initial minimizing crack ($A = 0.0810\,\text{mm}, R = 1.4311\,\text{mm}$), depicting a magnified region where the stress field exceeds ($\mathcal{F}(\mathbf{S}) \geq 0$) the strength surface of the material along with the test add-cracks of length ΔA oriented at angles β considered within. The line plot shows the variation of the energy $\mathcal{E}$ with respect to the add-crack angle β for $\Delta A = 0.05$ mm.

We now examine the minimizing solution with crack length $A = 0.0810$ mm at distance $R = 1.4311$ mm from the symmetry axis. At the critical applied displacement $u = u_{cr} = 0.0160$ mm, we numerically identify the region where the stress field violates the strength surface, $\mathcal{F}(\mathbf{S}) \geq 0$. Within this region, we introduce axisymmetric conical add-cracks of length ΔA, oriented at an angle β relative to the initial crack direction. This geometry yields a total crack surface area of $\mathcal{H}^2(\Gamma) = 2\pi RA + \pi\Delta A(2R + \Delta A \sin\beta)$. Our computations reveal that the energy $\mathcal{E}$ is minimized at $\Delta A = 0.05$ mm and $\beta = 32°$, indicating that the nucleated crack at $u = u_{cr}$ does not stay put but grows into a cone crack. Figure 19 illustrates the violation of the strength surface, depicts the add-cracks considered within, and plots the corresponding energy $\mathcal{E}$. Further computations show that subsequent crack propagation is stable, requiring an increase in the displacement u for the crack to continue growing. All of these findings are in agreement with the reference result.

5.5. Poker-chip test

Next, we turn to the 7$^{\text{th}}$ circle, the poker-chip test schematically illustrated in Fig. 20(a). The specimen consists of a circular disk of diameter $D = 10$ mm, whose bottom boundary is fixed to a flat substrate and top boundary is firmly bonded to a spherical fixture of radius $R = 18.2$ mm. The thickness of the disk

is therefore non-uniform, increasing radially from a centerline thickness of $L_c = 1$ mm to $L = 1.7$ mm at the outer edge. The spherical fixture is subjected to a prescribed vertical displacement u. For a nearly incompressible material — such as the synthetic rubber considered in this work — the applied displacement produces a non-homogeneous stress field within the disk characterized by a large hydrostatic component around its centerline. Under this stress state, a penny-shaped crack perpendicular to the loading direction nucleates near the centerline at a critical displacement u_{cr}.

Again, we begin by incrementally increasing the applied displacement u to numerically locate regions where the strength surface is violated, $\mathcal{F}(\mathbf{S}) \geq 0$. Such regions develop from the top boundary around the centerline of the specimen. For each displacement increment within these violation regions, the energy (6) is evaluated for specimens containing axisymmetric penny-shaped test cracks of radius A and at a distance H from the top boundary, corresponding to a crack surface area of $\mathcal{H}^2(\Gamma) = \pi A^2$; see Fig. 20(b). Figure 20(c) presents the resulting energy $\mathcal{E}$ as a function of A and H evaluated at the critical displacement $u = u_{cr} = 0.0637$ mm, the point at which a cracked configuration first minimizes the energy (6). Specifically, the energy at $u = u_{cr} = 0.0637$ mm is minimized by a crack of radius $A = 0.31$ mm located at a distance $H = 0.005$ mm from the top boundary, a finding that is in agreement with the reference result.

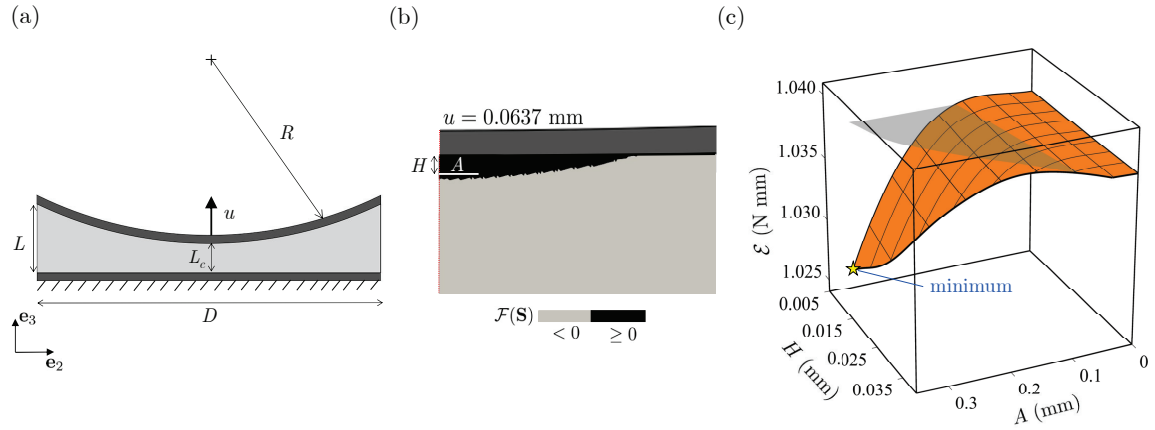


Figure 20: (a) Schematic of the poker-chip test on synthetic rubber. (b) Contour plot of a magnified region of the specimen where the stress field exceeds the strength surface of the material ($\mathcal{F}(\mathbf{S}) \geq 0$). The plot depicts the test cracks considered within this region and corresponds to $u = u_{cr} = 0.0637$ mm, the critical applied displacement at which a cracked configuration first minimizes the energy $\mathcal{E}$. (c) The corresponding energy $\mathcal{E}$ of the specimen as a function of the test crack radius A and distance H from the top boundary.

5.6. The double cantilever beam test

Having addressed all the circles in (Kamarei et al., 2026b) pertaining to fracture nucleation, we now turn to the 8$^{\text{th}}$ and 9$^{\text{th}}$ circles, which focus on fracture propagation under opening and tearing modes.

Figure 21(a) schematically illustrates the 8$^{\text{th}}$ circle, a double cantilever beam test. The specimen is a prismatic bar with dimensions $L = 55$ mm, $H = 20$ mm, and $B = 2.5$ mm, featuring a pre-existing edge crack of length $A = 25$ mm. To drive the growth of the crack, a displacement u is applied in the $\mathbf{e}_2$ direction through two pinholes. The corresponding resultant force is denoted by P. The pinholes have a radius of $B/8 = 0.3125$ mm, are positioned 1.5 mm inward from the left boundary, and are set at a vertical spacing of $H/3 = 6.6667$ mm between their centers. Increasing the applied displacement u causes the specimen arms to deform like cantilever beams. Once u reaches a critical value u_{cr}, self-similar crack growth ensues in the $\mathbf{e}_1$ direction. Further increase in the applied displacement u results in the stable propagation of the crack along the $\mathbf{e}_1$ direction.

To determine whether the proposed theory (5)-(7) yields predictions in agreement with the reference results, we begin by incrementally applying the displacement u and numerically identifying the regions where the strength surface is violated, $\mathcal{F}(\mathbf{S}) \geq 0$. As expected, these regions consistently localize around the crack front. At each displacement step, we determine the length ΔA of a straight, through-thickness

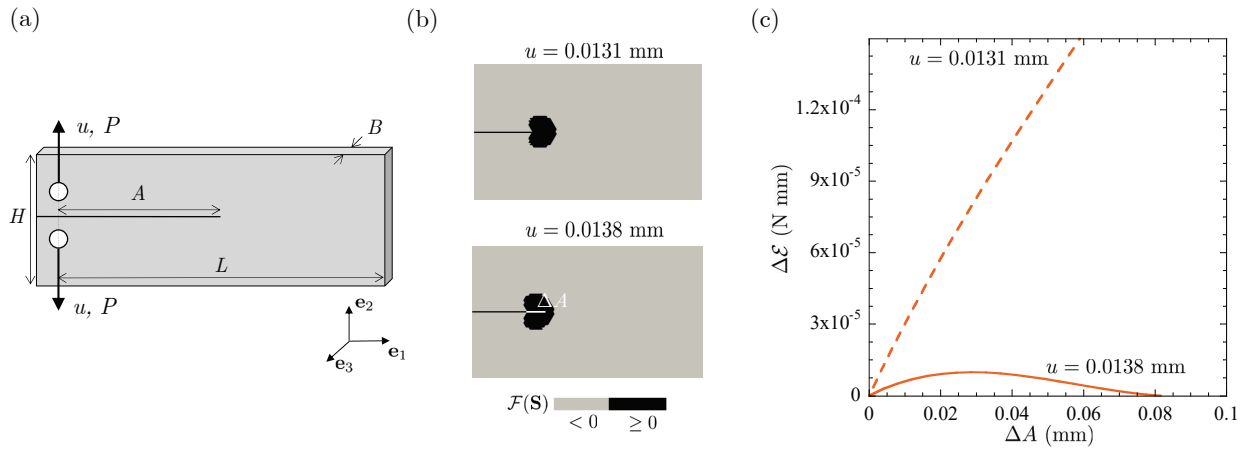


Figure 21: (a) Schematic of the double cantilever beam test on silicate glass. (b) Contour plots of magnified regions where the strength surface is violated ($\mathcal{F}(\mathbf{S}) \geq 0$), illustrating the considered test add-cracks, at two applied displacements u. (c) The corresponding energy difference $\Delta\mathcal{E} = \mathcal{E} - \mathcal{E}|_{\Delta A=0}$ plotted as a function of the add-crack length ΔA.

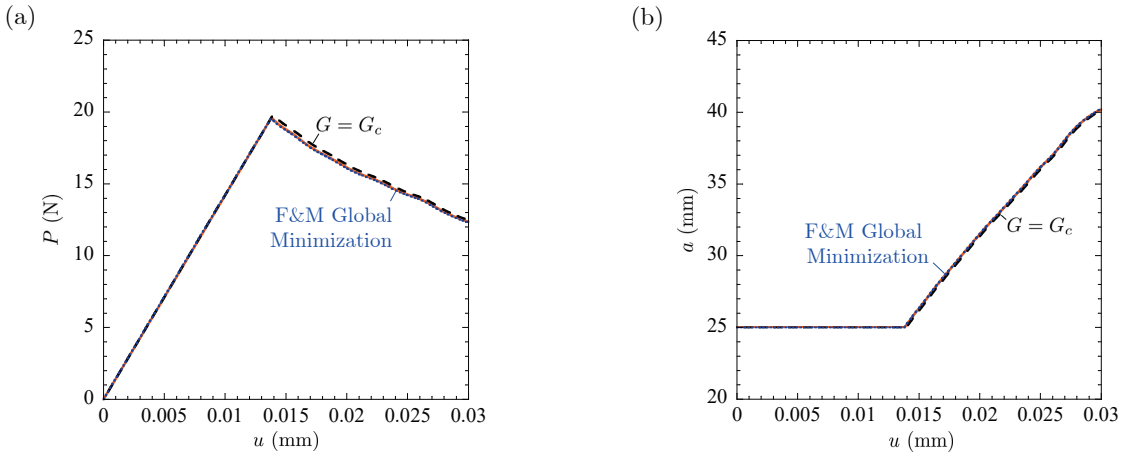


Figure 22: Theoretical predictions (solid lines) for the double cantilever beam test. (a) The force-displacement response. (b) The associated evolution of crack length a. For direct comparison, both plots include the predictions (dashed and dotted lines) associated with the classical Griffith criterion, $G = G_c$, and the Francfort-Marigo global energy minimization.

add-crack (with surface area $\mathcal{H}^2(\Gamma) = \Delta AB$) that minimizes the energy (6). The search is restricted to self-similar test add-cracks with straight fronts. We checked that kinked trajectories do not yield energy minimizers and that, due to the small specimen thickness ($B = 2.5$ mm), curved crack fronts through the thickness have a minor effect on $\mathcal{E}$. Figure 21 shows contour plots of magnified strength-violation regions for two displacements, $u = 0.0131$ mm and 0.0138 mm, and depicts the test add-cracks considered within these regions. As shown in Fig. 21(c), the value $u = 0.0138$ mm corresponds to the critical displacement u_{cr} at which an add-crack first minimizes (6) — that is, the displacement at which the pre-existing crack begins to grow. Importantly, the minimizing crack is small but of a finite length $\Delta A = 0.08$ mm.

Repeating the computation on the updated geometry with a crack length of $a = A + \Delta A = 25.08$ mm reveals that the crack propagates by another jump of $\Delta A = 0.08$ mm as the displacement increases to $u = 0.0139$ mm. This stable propagation via small jumps — and *not* via a time-continuous smooth growth as commonly assumed — continues as u increases further. The results, plotted in Fig. 22, confirm that these

predictions are in agreement with the reference results.

For direct comparison, Fig. 22 includes the predictions of the classical Griffith criterion — which dictates that crack propagation occurs when the energy release rate reaches the fracture toughness, $G = G_c$ — alongside those generated by the global energy minimization approach of Francfort and Marigo (1998). We emphasize that the classical Griffith criterion restricts add-cracks to be infinitesimally small, assuming that crack growth is a time-continuous smooth process. By contrast, global energy minimization places no restrictions on the size of add-cracks. Accordingly, it allows for growth by jumps — much like the theory proposed herein — which is precisely what it predicts for this test (specifically, jumps of 0.10 mm).

A key observation from Fig. 22 is that all three sets of predictions are qualitatively and quantitatively similar for this specific problem, as the jumps predicted by both the proposed theory and global energy minimization are small. Consequently, isolated use of this type of double cantilever beam test cannot provide meaningful experimental validation.

5.7. The trousers test

Finally, Fig. 23(a) shows a schematic of the 9$^{\text{th}}$ circle, a trousers test. The specimen, made of the synthetic rubber investigated in this work, consists of a rectangular sheet of length $L = 100$ mm, width $H = 40$ mm, and thickness $B = 1$ mm containing a pre-existing edge crack of initial length $A = 50$ mm. Loading is initiated by bending the two legs in opposite directions to align them in a coplanar configuration. The lower ends of the legs are firmly gripped and subjected to an imposed separation l along the $\mathbf{e}_2$ direction, generating a resultant reaction force P. As the separation l increases, the legs of the trousers undergo elastic stretching, bending, and twisting. Once a critical separation between the grips, l_{cr}, is reached, the crack begins to propagate in a self-similar manner along the $\mathbf{e}_3$ direction. Further increases in l result in stable crack growth along $\mathbf{e}_3$.

The application of the proposed theory (5)-(7) follows the procedure used for the preceding circle. We incrementally apply the grip-to-grip separation l and computationally identify the regions of strength violation, $\mathcal{F}(\mathbf{S}) \geq 0$. These regions localize tightly near the crack front. For each separation increment, we calculate the length ΔA of a straight through-thickness add-crack (with surface area $\mathcal{H}^2(\Gamma) = \Delta A B$) that minimizes the energy (6). Again, restricting our scope to these specific topologies is justified since kinked paths are not energy minimizers and, owing to the thinness of the specimen ($B = 1$ mm), through-thickness curved fronts barely alter $\mathcal{E}$. Figure 23 presents a magnified contour plot of the strength-violation region at $l = 98.5$ mm, overlaying the test add-cracks evaluated within. As shown in Fig. 23(c), this specific separation

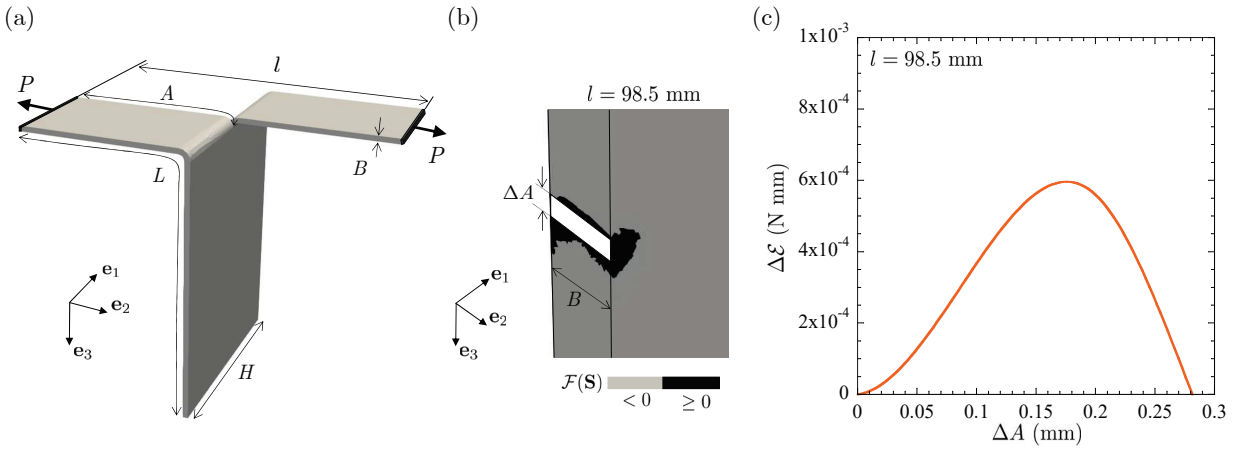


Figure 23: (a) Schematic of the trousers test on synthetic rubber. (b) Contour plot of a magnified region where the strength surface is violated ($\mathcal{F}(\mathbf{S}) \geq 0$), illustrating the considered test add-cracks, at the separation between the grips $l = l_{cr} = 98.5$ mm. (c) The corresponding energy difference $\Delta\mathcal{E} = \mathcal{E} - \mathcal{E}|_{\Delta A=0}$ plotted as a function of the add-crack length ΔA.

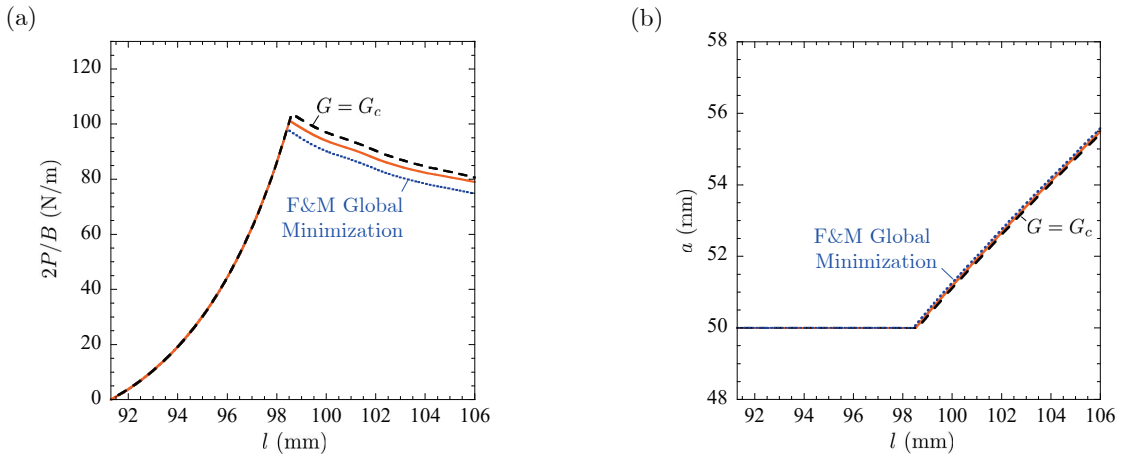


Figure 24: Theoretical predictions (solid lines) for the trousers test. (a) The normalized force $2P/B$ as a function of the applied separation l between the grips. (b) The associated evolution of crack length a. For direct comparison, both plots include the predictions (dashed and dotted lines) associated with the classical Griffith criterion, $G = G_c$, and the Francfort-Marigo global energy minimization.

corresponds to the critical value l_{cr} at which an add-crack first minimizes (6). Importantly, the minimizing crack is small but distinctly finite, measuring $\Delta A = 0.28$ mm.

Subsequent calculations on the updated configuration — now with a crack length of $a = A + \Delta A = 50.28$ mm — show a second discrete advancement of $\Delta A = 0.28$ mm once the grip-to-grip separation reaches $l = 98.86$ mm. This stable step-wise crack propagation — and, once again, *not* via a time-continuous smooth growth as commonly assumed — persists under continued loading. These findings, plotted in Fig. 24, are in agreement with the reference results.

As in the previous case, we have included in Fig. 24 the theoretical predictions from both the classical Griffith criterion and the global energy minimization of Francfort and Marigo (1998) for direct comparison. We reiterate the fundamental distinction here: the classical Griffith criterion restricts add-cracks to be infinitesimally small, whereas the global energy minimization approach of Francfort and Marigo (1998) imposes no add-crack size constraints. The conclusions and implications mirror those noted for the double cantilever beam test.

6. Final comments

The ability to predict when and where fracture nucleates and propagates under arbitrary loading conditions has long stood as a major hurdle in solid mechanics. The broad range of results presented in the preceding section suggests that the proposed theory provides a satisfactory answer. Further validation should confirm the generality of the theory. Specifically, validation for problems where fracture is driven by body forces — such as gravity — should prove valuable, as very few benchmark studies of this type currently exist.

Of the three intrinsic material properties entering the theory — the elastic energy density $W(\mathbf{F})$, the strength surface $\mathcal{F}(\mathbf{S}) = 0$, and the fracture toughness G_c — the strength surface is arguably the most challenging to measure in its entirety through direct experiments, although, in all fairness, characterizing the complete $W(\mathbf{F})$ for a nonlinear elastic material presents a comparable challenge. This stems from the practical difficulty of subjecting specimens to spatially uniform stress states that span the entire stress space. Nevertheless, because the strength surface strictly constrains where fracture can occur, experiments featuring non-uniform stress fields can now be leveraged. Specifically, the entire strength surface $\mathcal{F}(\mathbf{S}) = 0$ can be identified via inverse calibration, tuning its parameters so that theoretical predictions match macroscopic experimental observations.

Deriving the time-continuous limit of the proposed sharp formulation is key. So is the development of phase-field and other diffuse regularizations. In particular, it would be highly valuable to establish whether the phase-field theory introduced in (Kumar, Francfort and Lopez-Pamies, 2018a) — which directly motivated the theory proposed here — provides a mathematically rigorous regularization of the sharp formulation, one where the driving force c_{e} introduced in that formulation plays the role of a penalty term that enforces the strength surface constraint.

Developing an efficient and robust numerical implementation of the proposed theory represents another crucial priority. The physical constraint imposed by the strength surface should render the computations highly tractable, even when explicitly tracking sharp cracks. This holds particularly true for initial-boundary-value problems that can be treated in 2D.

Acknowledgements

The work of the first two authors was supported by the National Science Foundation through the Grants DMS–2308169 and CMMI–2132528. This support is gratefully acknowledged.

References

Ambrosio, L., Fusco, N., Pallara, D., 2000. Functions of Bounded Variation and Free Discontinuity Problems. Oxford University Press, Oxford.

Ambrosio, L., Tilli, P., 2004. Topics on Analysis in Metric Spaces. Oxford University Press, Oxford.

Beer, F., Johnston, E.R., Dewolf, J., Mazurek, D., 2019. Mechanics of Materials. McGraw-Hill Education.

Bourdin, B., Francfort, G.A., Marigo, J.J., 2008. The variational approach to fracture. Journal of Elasticity 91, 5–148.

Breedlove, E., Chen, C., Lindeman, D., Lopez-Pamies, O., 2024. Cavitation in elastomers: A review of the evidence against elasticity. Journal of the Mechancis and Physics of Solids 188, 105678.

Budiansky, B., Rice, J.R., 1973. Conservation laws and energy-release rates. Journal of Applied Mechanics 40, 201–203.

Cauchy, A.L., 1823. Recherches sur l'équilibre et le mouvement intérieur des corps solides ou fluides, élastiques ou non élastiques. Bulletin ile la Société Philomatique , 9–13.

Cauchy, A.L., 1828. Sur les équations qui expriment l'équilibre ou les lois du mouvement intérieur d'un corps solide élastique ou non élastique. Exercices de Mathématiques , 195–226.

Chambolle, A., Francfort, G.A., Marigo, J.J., 2009. When and how do cracks propagate? Journal of the Mechanics and Physics of Solids 57, 1614–1622.

Chambolle, A., Francfort, G.A., Marigo, J.J., 2010. Revisiting energy release rates in brittle fracture. Journal of Nonlinear Science 20, 395–424.

Chambolle, A., Giacomini, A., Ponsiglione, M., 2008. Crack initiation in brittle materials. Archive for Rational Mechanics and Analysis 188, 309–349.

Cornetti, P., Pugno, N., Carpinteri, A., Taylor, D., 2006. Finite fracture mechanics: A coupled stress and energy failure criterion. Engineering Fracture Mechanics 73, 2021–2033.

Crouzeix, M., Raviart, P.A., 1973. Conforming and nonconforming finite element methods for solving the stationary Stokes equations. R.A.I.R.O. R3, 33–76.

Dal Maso, G., Francfort, G.A., Toader, R., 2005. Quasistatic crack growth in nonlinear elasticity. Archive for Rational Mechanics and Analysis 176, 165–225.

Davenport, J.C.W., Smith, D.J., 1993. A study of superimposed fracture modes I, II, and III on PMMA. Fatigue and Fracture of Engineering Materials and Structures 16, 1125–1133.

Erdogan, G., Sih, G.C., 1963. On the crack extension in plates under plane loading and transverse shear. Journal of Basic Engineering 85, 519–527.

Evans, L.C., Gariepy, R.F., 1992. Measure Theory and Fine Properties of Functions. CRC Press, Boca Raton.

Francfort, G.A., Giacomini, A., Lopez-Pamies, O., 2019. Fracture with healing: A first step towards a new view of cavitation. Analysis and PDE 12, 417–447.

Francfort, G.A., Larsen, C.J., 2003. Existence and convergence for quasi-static evolution in brittle fracture. Communications on Pure and Applied Mathematics 56, 1465–1500.

Francfort, G.A., Marigo, J.J., 1998. Revisiting brittle fracture as an energy minimization problem. Journal of the Mechanics and Physics of Solids 46, 1319–1342.

Goldstein, R.V., Salganik, R.L., 1974. Brittle fracture of solids with arbitrary cracks. International Journal of Fracture 10, 507–523.

Green, G., 1838. On the laws of reflection and refraction of light at the common surface of two non-crystallized media. Transactions of the Cambridge Philosophical Society 7, 245–269.

Griffith, A.A., 1921. The phenomena of rupture and flow in solids. Philos. Trans. R. Soc. Lond. Ser. A 221, 163–198.

Griffith, A.A., 1924. The theory of rupture, in: Proceedings of the First International Congress for Applied Mechanics, Delft.

Hua, W., Li, J., Zhu, Z., A.Li, Huang, J., Gan, Z., Dong, S., 2023. A review of mixed mode I-II fracture criteria and their applications in brittle or quasi-brittle fracture analysis. Theoretical and Applied Fracture Mechanics 124, 103741.
Irwin, G.R., 1948. Fracture dynamics, in: Fracturing of Metals. American Society For Metals, Cleveland. pp. 147–166.
Irwin, G.R., 1957. Analysis of stresses and strains near the end of a crack traversing a plate. Journal of Applied Mechanics 24, 361–364.
Kamarei, F., Breedlove, E., Lopez-Pamies, O., 2025. Validating Griffith fracture propagation in the phase-field approach to fracture: The case of Mode III by means of the trousers test. International Journal of Fracture 249, 51.
Kamarei, F., Bueno De Castro, S., Roesler, J.R., Lopez-Pamies, O., 2026a. Fracture under body forces: An accessible test and analysis. In preparation .
Kamarei, F., Kumar, A., Lopez-Pamies, O., 2024. The poker-chip experiments of synthetic elastomers explained. Journal of the Mechanics and Physics of Solids 188, 105683.
Kamarei, F., Zeng, B., Dolbow, J.E., Lopez-Pamies, O., 2026b. Nine circles of elastic brittle fracture: A series of challenge problems to assess fracture models. Computer Methods in Applied Mechanics and Engineering 448, 118449.
von Kármán, T., 1911. Festigkeitsversuche unter allseitigem druck [Strength tests under hydrostatic pressure]. Zeitschrift des Vereines Deutscher Ingenieure 55, 1749–1757.
Knowles, J.K., Sternberg, E., 1972. On a class of conservation laws in linearized and finite elastostatics. Archive for Rational Mechanics and Analysis 44, 187–211.
Knowles, J.K., Sternberg, E., 1973. An asymptotic finite-deformation analysis of the elastostatic field near the tip of a crack. Journal of Elasticity 3, 67–107.
Kumar, A., Bourdin, B., Francfort, G.A., Lopez-Pamies, O., 2020. Revisiting nucleation in the phase-field approach to brittle fracture. Journal of the Mechanics and Physics of Solids 142, 104027.
Kumar, A., Francfort, G.A., Lopez-Pamies, O., 2018a. Fracture and healing of elastomers: A phase-transition theory and numerical implementation. Journal of the Mechanics and Physics of Solids 112, 523–551.
Kumar, A., Liu, Y., Dolbow, J.E., Lopez-Pamies, O., 2024. The strength of the Brazilian fracture test. Journal of the Mechanics and Physics of Solids 182, 105473.
Kumar, A., Lopez-Pamies, O., 2020. The phase-field approach to self-healable fracture of elastomers: A model accounting for fracture nucleation at large, with application to a class of conspicuous experiments. Theoretical and Applied Fracture Mechanics 107, 102550.
Kumar, A., Lopez-Pamies, O., 2021. The poker-chip experiments of Gent and Lindley (1959) explained. Journal of the Mechanics and Physics of Solids 150, 104359.
Kumar, A., Ravi-Chandar, K., Lopez-Pamies, O., 2018b. The configurational-forces view of fracture and healing in elastomers as a phase transition. International Journal of Fracture 213, 1–16.
Kumar, A., Ravi-Chandar, K., Lopez-Pamies, O., 2022. The revisited phase-field approach to brittle fracture: Application to indentation and notch problems. International Journal of Fracture 237, 83–100.
Lamé, G., 1852. Leçons Sur la Théorie Mathématique de l'élasticité des Corps Solides. Mallet-Bachelier.
Lamé, G., Clapeyron, E., 1831. Mémoire sur l'équilibre intérieur des corps solides homogènes. Journal für die reine und angewandte Mathematik 7, 381–413.
Larsen, C.J., 2021. Variational fracture with boundary loads. Applied Mathematics Letters 121, 107437.
Larsen, C.J., 2024. A local variational principle for fracture. Journal of the Mechanics and Physics of Solids 187, 105625.
Larsen, C.J., Dolbow, J.E., Lopez-Pamies, O., 2024. A variational formulation of Griffith phase-field fracture with material strength. International Journal of Fracture 247, 319–327.
Lefèvre, V., Lopez-Pamies, O., 2017. Nonlinear electroelastic deformations of dielectric elastomer composites: II — Non-Gaussian elastic dielectrics. Journal of the Mechanics and Physics of Solids 99, 438–470.
Lefèvre, V., Ravi-Chandar, K., Lopez-Pamies, O., 2015. Cavitation in rubber: An elastic instability or a fracture phenomenon? International Journal of Fracture 192, 1–23.
Leguillon, D., 2002. Strength or toughness? A criterion for crack onset at a notch. European Journal of Mechanics-A/Solids 21, 61–72.
Lopez-Pamies, O., Kamarei, F., 2025. When and where do large cracks grow? Griffith energy competition constrained by material strength. Extreme Mechanics Letters 81, 102417.
Love, A.E.H., 1906. A Treatise on the Mathematical Theory of Elasticity. Cambridge University Press, Cambridge University Press.
Mahajan, R.V., Ravi-Chandar, K., 1989. An experimental investigation of mixed-mode fracture. International Journal of Fracture 41, 235–252.
Mohr, O., 1900. Welche umstände bedingen die elastizitätsgrenze und den bruch eines materiales? [What circumstances determine the elastic limit and fracture of a material?]. Zeitschrift des Vereines deutscher Ingenieure 44, 1524–1530,1572–1574.
Navier, C.L., 1827. Mémoire sur les lois de l'équilibre et du mouvement des corps solides élastiques. Mémoires de l'Académie Royale des Sciences de l'Institut de France 7, 375–393.
Navier, C.L., 1864. Résumé des leçons données à l'École des ponts et chaussées sur l'application de la mécanique à l'établissement des constructions et des machines. 3 ed., Dunod, Paris.
Nuismer, R.J., 1975. An energy release rate criterion for mixed mode fracture. International Journal of Fracture 11, 245–250.
Orowan, E., 1948. Fracture and strength of solids. Reports on Progress in Physics 12, 185–232.
Palaniswamy, K., Knauss, W.G., 1978. On the problem of crack extension in brittle solids under general loading, in: Mechanics Today, pp. 87–148.
Panasyuk, V.V., Berezhnitskiy, L.T., Kovchik, S.Y., 1965. Propagation of an arbitrarily oriented rectilinear crack during

extension of a plate. Prikladnaya Mekhanika 1, 48–55.
Qian, J., Fatemi, A., 1996. Mixed mode fatigue crack growth: A literature survey. Engineering Fracture Mechanics 55, 969–990.
Rankine, W.J.M., 1858. A Manual of Applied Mechanics. Richard Griffin and Company.
Rice, J.R., 1966. An examination of the fracture mechanics energy balance from the point of view of continuum mechanics, in: Proceedings of the First International Conference on Fracture, Sendai. pp. 309–340.
Rice, J.R., 1968. A path independent integral and approximate analysis of strain concentration by notches and cracks. Journal of Applied Mechanics 35, 379–386.
Richard, H.A., 1985. Fracture predictions for cracks exposed to superimposed normal and shear stresses [Bruchvorhersagen bei überlagerter Normal-und Schubbeanspruchung von Rissen]. VDI-Forschungsheft 631, 60.
Richard, H.A., Schramm, B., Schirmeisen, N.H., 2014. Cracks on mixed mode loading — Theories, experiments, simulations. International Journal of Fatigue 62, 93–103.
Rivlin, R.S., 1948a. Large elastic deformations of isotropic materials. I. Fundamental concepts. Philosophical Transactions of the Royal Society of London. Series A 240, 459–490.
Rivlin, R.S., 1948b. Large elastic deformations of isotropic materials. IV. Further developments of the general theory. Philosophical Transactions of the Royal Society of London. Series A 241, 379–397.
Rivlin, R.S., Thomas, A.G., 1953. Rupture of rubber. I. Characteristic energy for tearing. Journal of Polymer Science 10, 291–318.
Royer, J., 1986. A specimen geometry for plane mixed mode. Engineering Fracture Mechanics 23, 763–775.
Saha, S., Dolbow, J.E., Lopez-Pamies, O., 2024. A Griffith description of fracture for non-monotonic loading with application to fatigue. Journal of the Mechanics and Physics of Solids 191, 105754.
Saha, S., Manaughand, B., Moore, B.J., Roesler, J.R., Lopez-Pamies, O., 2026a. A guide to fully characterize the fracture properties of cementitious materials from simple experiments. Submitted .
Saha, S., Roesler, J.R., Lopez-Pamies, O., 2026b. Breaking four-point and three-point bending tests. International Journal of Solids and Structures 339, 114169.
Sih, G.C., 1974. Strain-energy-density factor applied to mixed mode crack problems. International Journal of Fracture 10, 305–321.
Tada, H., Paris, P., Irwin, G., 1973. The stress analysis of cracks handbook 3rd edition. The American Society of Mechanical Engineers, New York.
Theocaris, P.S., Andrianopoulos, N., 1982. A modified strain-energy density criterion applied to crack propagation. Journal of Applied Mechanics 49, 81–86.
Tian, D.C., Lu, D.Q., Zhu, J.J., 1982. Crack propagation under combined stresses in three dimensional medium. Engineering Fracture Mechanics 16, 5–16.
Truesdell, C., Noll, W., 1965. The Non-Linear Field Theories of Mechanics. Springer.
Ueda, Y., Ikeda, K., Yao, T., Aoki, M., 1983. Characteristics of brittle fracture under general combined modes including those under bi-axial tensile loads. Engineering Fracture Mechanics 18, 1131–1158.
Williams, J.G., Ewing, P.D., 1972. Fracture under complex stress — The angled crack problem. International Journal of Fracture Mechanics, 8, 441–446.
Wu, C.H., 1978. Fracture under combined loads by maximum-energy-release-rate criterion. Journal of Applied Mechanics 45, 553–558.